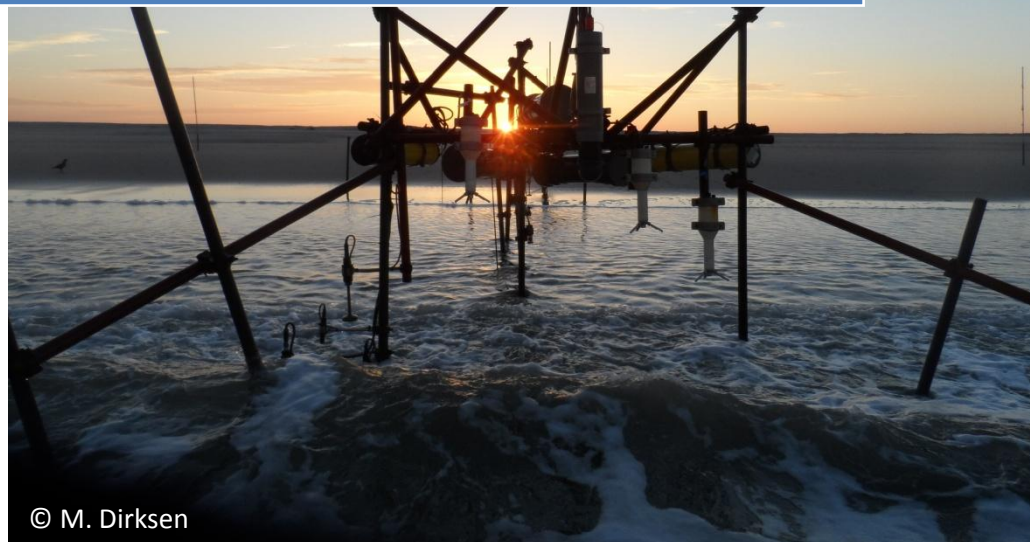


2015

Ripple Characteristics in the Intertidal Area

Field measurements at the Sand Motor, The Netherlands



© M. Dirksen

Marieke Dirksen

Supervision: Joost Brinkkemper and Gerben

Ruessink

University of Utrecht, Department of
physical geography. Master Thesis.

3-11-2015

Abstract

The first 3D sonar field measurements of ripples in the intertidal area are presented. The measurements were conducted during a 6 week field campaign in Autumn 2014 at the Sand Motor near Den Hague, The Netherlands. Ripple profile, hydrodynamic and suspension data were collected along a cross-shore transect. By means of a 2D Fourier analysis the 3D sonar images of the bedforms were analysed. Key parameters such as ripple height, length and angle were obtained. These parameters correlate to one another as well as to hydrodynamic data. During the measurement period the wave conditions were mostly calm and most waves arrived shore normal. A correlation between relative wave height and ripple length is found. The estimated ripple index, of 17.1, corresponds well to values found in literature. The FFT-routines are a powerful tool for analysing the enormous amount of sonar data, 1100 3D-images, automatically. A rotational diagram method was used to analyse 3D sonar images. A ripple regularity index (RRI) is proposed, as an objective and quantitative way to classify a ripple pattern as 'regular' or 'irregular'.

Keywords: Ripples, Sonar, Sand Motor, Hydrodynamics, FFT, Rotational diagram, Ripple Regularity Index

Table of Content

Abstract.....	2
1. Introduction	4
2. Literature Background	5
2.1 An introduction: terminology and ripple types	5
2.1.1 Wave ripples.....	7
2.1.2 Mega ripples.....	8
2.2 Ripple classification	9
2.2.1 The Classification of Clifton (1976).....	9
2.2.2 The Classification of Dumas 2005	11
2.2.3 Modern ripple predictions: Goldstein et al, 2013 and Nelson et al, 2013	13
2.2.4 Classification of co-existing ripples	15
3. Problem definition and research questions & aims.....	16
4. Methods.....	17
4.1. Data Collection	17
4.2. Data Processing	21
4.2.1 Two dimensional ripple images: Line scans	21
4.2.2 Sonar Images in 3D.....	21
4.2.3 Hydrodynamic data	23
4.3. Data Analysis	24
4.3.1 Ripple characteristics	24
4.3.2 Fourier analysis: the basics.....	24
4.3.3 Effect of the Loess filter settings on the Ripple Amplitude.....	26
4.3.4 Examples of the dataset.....	28
4.3.5 The Ripple Regularity Index (RRI)	30
4.3.6 Hydrodynamic parameters.....	33
5. Results.....	35
5.1 Overview of the dataset	35
5.2 Ripple Index	39
5.3 Overview of the Ripple Regularity Index	40
5.4 Ripple classification	42
6. Discussion	44
7. Conclusion.....	48
Acknowledgements.....	49
References	50

1. Introduction

The Sand Motor is a man-made peninsula of 1 km² at the Delfland Coast. The Sand Motor is a unique experiment where the dynamic coastline is managed and enforced. According to the old enforcement method, the Dutch coastline is artificially replenished with sand, approximately every 5 years. The Sand Engine has potential economical and ecological benefits, and has a estimated maintenance cycle of 20 years. The waves and currents spread its sand along the coast. This is called 'Building with Nature'. A similar project to another weak coastal area has started: the Hondsbossche seawall near Petten (www.dezandmotor.nl).

Coastal safety is essential for the Netherlands, especially considering the relative sea level rise. Sediment transport plays an important role for the protection of the coast. The knowledge on sediment transport, especially in the surf zone, is limited. Many factors, such as waves and currents, influence the sediment fluxes, which makes the problem very complicated. In deeper water the bed morphology can be predicted with the oscillatory flow. In the surf zone the process becomes more complicated. Ripples can change the phase-coupling between short wave orbital motion and suspension, and thus affect sediment transport. Besides the timing, bedforms also influence the magnitude of the sediment transport (Van Rijn et al., 2013).

The hydrodynamics and morphodynamics in the surf-zone are closely related (Van Rijn et al., 2013). Small scale structures, such as ripples, have a great influence on the sediment transport (e.g. Nielsen, 1992 ; Van Rijn et al., 2013). To be able to predict coastal change, knowledge about the interaction between hydrodynamics and morphodynamics is crucial. There is however still a gap in our knowledge and understanding of sand transport in the surf-zone (Van Rijn et al., 2013). Measurements of small scale morphology are needed to determine their influence on the hydrodynamics (Thornton et al. 1998).

Ripples can be further classified as: wave ripples, current ripples and mega ripples. Under shoaling waves, wave ripples are formed, under low energy conditions. Due to alongshore currents, or an undertow, current ripples can form. With storm conditions, and low energy conditions, megaripples can form (Gallagher, 2003). It is also possible to find various bedforms superimposed on one another. In case of an oscillatory flow and a unidirectional flow, both wave ripples and current ripples can co-exist, as well as mega ripples and wave ripples (Masselink et al. 2007).

As field measurements are scarce and the morphodynamics of the surf zone are poorly understood, fieldwork was conducted at the Sand Motor. This master thesis will focus on the data analysis and characterisation of ripples, as well as the correlation to wave parameters.

This Thesis is organised as follows: an overview of relevant literature is given in section 2 'Literature Background', here the ripple types and ripple classification methods are discussed. The classification of *Clifton, 1976* is as good as the ripple predictors of *Goldstein et al., 2013* and *Nelson et al., 2013*. They found relations between ripple parameter and hydrodynamic conditions. Section 3 describes the research goal: '*Provide a ripple characterisation methods, applicable to the intertidal zone, and relate ripple parameters to hydrodynamic conditions.*' Section 4 describes methods: data collection (fieldwork), data processing (3D sonar image reconstruction) and data analysis, involving a Fast Fourier Transform (FFT) and a rotational diagram method. The characteristic ripple parameter, such as height, length, angle and Ripple Regularity Index (RRI) are obtained. In section 5 'Results' a benchmark of this study to literature findings is provided. Correlations and data trends of the various ripple parameters are shown. Finally the FFT results are compared with the rotational diagram method. Sections 6 and 7 contain the discussion, conclusion and recommendations for future research.

2. Literature Background

The field measurements were mainly collected in intermediate and shallow water. Therefore this chapter will discuss the nearshore bedforms, with a focus on intermediate and shallow water. The terminology and main ripple characteristics are presented in chapter 2.1. Chapter 2.2 continues with a classification of the ripples: the model of *Clifton 1976* and the classification of *Dumas et al. 2005* will be discussed. The most recent prediction methods for ripples are of *Goldstein et al., 2013* and *Nelson et al., 2013*.

2.1 An introduction: terminology and ripple types

The nearshore zone is composed of complex bedforms, as the waves and currents are highly variable (*Thornton et al. 1998*). The nearshore can be subdivided in four zones, namely: deep water, intermediate and shallow water, surf zone and swash zone. In deep water waves are unaffected by the seabed. In intermediate and shallow water waves are affected by the sea bed and wave shoaling occurs. In the surf zone the waves are breaking. In the swash zone the waves runup the beach, called wave runup (*Masselink, 2011*).

The type of bedform is both time and space depended. Flow strength is very important as it moves sediments. The nature of the flow determines the shape of the bedforms. Only oscillatory flow will result in regular, long crested vortex ripples. These ripples are found seawards of the breaker zone and in the trough, behind the bar (Figure 1). In the breaker zone mega ripples or flat bed are found, this is due to the turbulence (*Nielsen, 1992*). The ripples expected during the fieldwork are mainly vortex ripples and mega ripples.

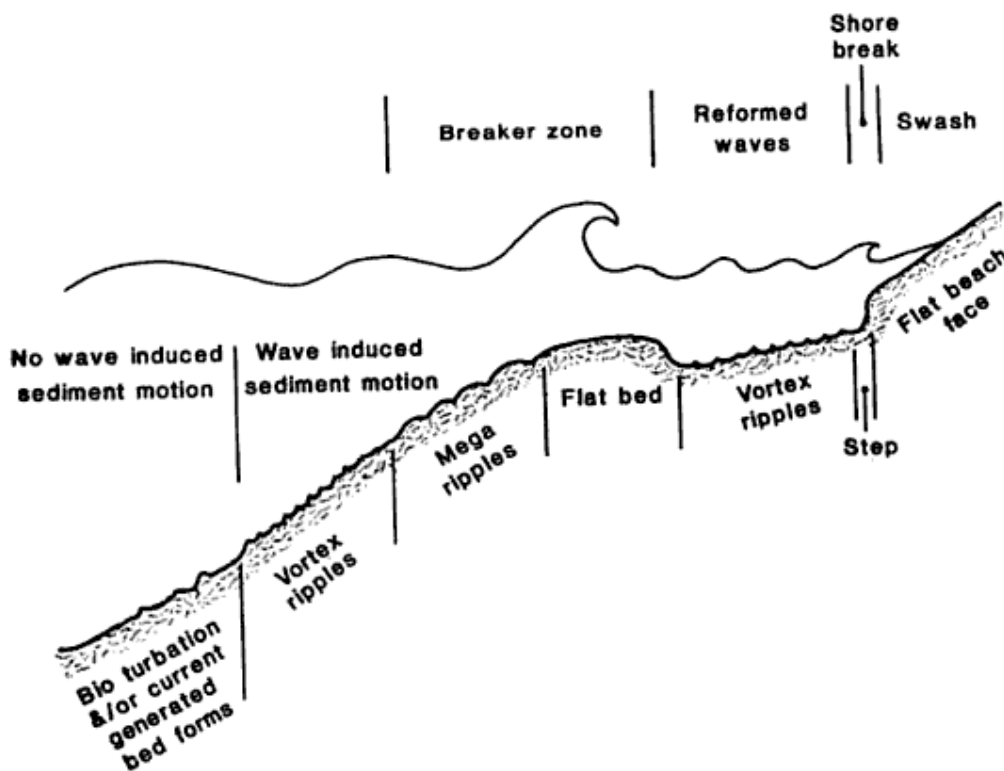


Figure 1. Bedform distribution on an barred beach. In deep water bio turbation and/or current generated bedforms are present. Oscillatory flow forms vortex ripples outside the breaker zone and behind the bar, where waves are reformed. In the breaker zone megaripples and a flat bed is found (*Nielsen, 1992*).

The ripple terminology, used by *Dumas et al. (2005)*, is presented in Figure 2. The crest of the ripple is the highest point, the trough is the lowest point. The length from one trough to the other trough is defined as the wavelength. The height is defined as the height difference between the crest and trough of the ripple. The ripple index (RI) is the wavelength divided by the height. The symmetry index is calculated by dividing the stoss side (from the trough to the brinkpoint) and the lee side (from the brinkpoint to the trough). These terms will be used later on during the analysis of field data.

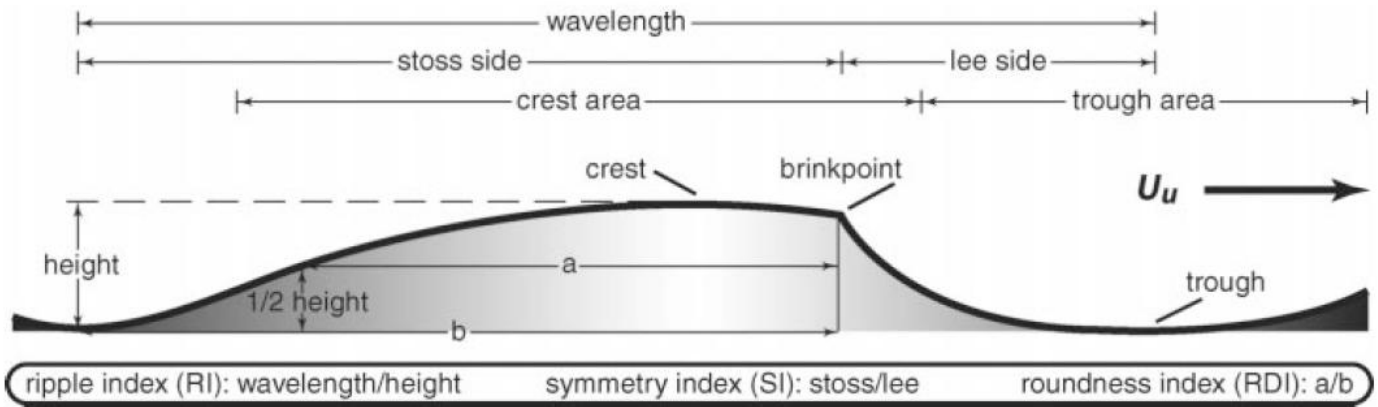


Figure 2. A schematic cross section of a ripple with terminology (Dumas et al., 2005).

The example in Figure 2 is a current ripple (length ~20cm, height ~2cm). Current ripples at the beach can be associated with longshore currents, rip currents or an undertow (Thornton et al., 1998). Longshore currents are expected to generate transverse bedforms, like linguoid or irregular ripples (Hunter et al., 1979). Current ripples are not expected to be recorded during the fieldwork. Wave ripples and mega ripples are and will be described in the next two subchapters (2.1.1 & 2.1.2).

2.1.1 Wave ripples

Wave ripples have a typical length of 20cm and a height of 2cm. Wave ripples can be recognised by their straight or concave-up stoss and lee sides. The trough of the ripple is broad. The brinkpoints are mostly continuous and at the same position as the crest line (Dumas et al., 2005). Wave ripples also have ramifications of the crest line and are associated with oscillatory flow (Ruessink et al., 2011). Steeper ripples cause sediment suspension higher in the water column (e.g. Osborne et al., 1996; Fredsøe et al., 1999; Gigoriadis et al., 2012). Under the same wave conditions the suspended sediment transport shows large differences depending on the presence or absence of bedforms (Osborne et al., 1996).

Vortex ripple, a type of wave ripples, influence the sediment transport considerably. The suspended sediment distribution scales with the ripple height. The scale of the vortex ripple is closely related to the wave environment. Figure 3 shows the relation between the length of the vortex ripple and the wave induced motion. Vortex ripples are sharp crested ($\eta/\lambda=0.15$) they develop under calm wave energy conditions (Bagnold, 1963). To calculate the wave induced motion the significant wave height or Root mean square (*rms*) wave height is often used (Nielsen, 1992).

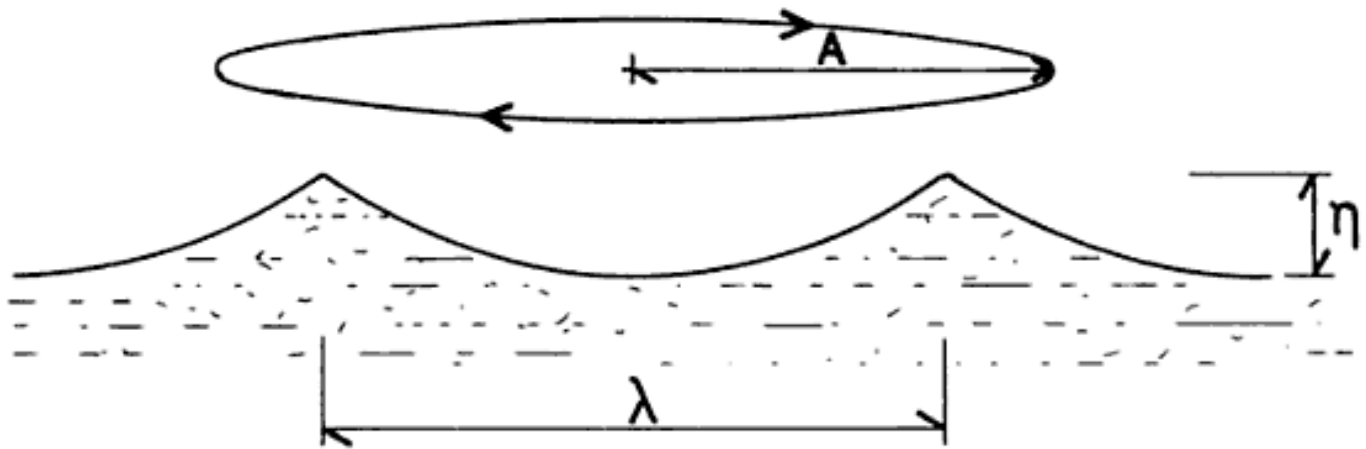


Figure 3. Example of a vortex ripple and the orbit length (λ =ripple length, η =ripple height, A =orbit length). The length of this ripple is closely related to the wave induced motion near the bed (Nielsen, 1992).

2.1.2 Mega ripples

Megaripples have a wavelength of 1-5m and a height of 10-50cm. Megaripples have no brinkpoint (Dumas et al., 2005). Gallagher et al. (2003) observed different types of megaripples. It was suggested that these features are present during storm and lower-energy conditions. During these low energy conditions they can be present inside the surf zone (Hunter et al., 1979). It is even suggested that they probably occur frequently in the surf zone (Gallagher, 2003). During laboratory experiments, with oscillatory and unidirectional flow, megaripples were investigated. In Figure 4 two types of megaripples are shown: reverse large ripple and asymmetric large ripple. Under high oscillatory flow conditions and low unidirectional flow conditions reverse large ripples develop. If the unidirectional flow is larger asymmetric large ripples develop (Dumas et al. 2005). Under high unidirectional flow conditions megaripples resemble dunes (Gallagher, 2003; Dumas et al., 2005).

Recent field measurements showed that both megaripples and wave ripples can co-exist (Miles, 2013). Also wave and current ripples can co-exist. These bedforms form under conditions with both wave and currents, more specific, they are formed due to a combination of oscillatory flow and mean flow (Blondeaux, 2000). The co-existence of megaripples and wave ripples has been observed during the fieldwork.

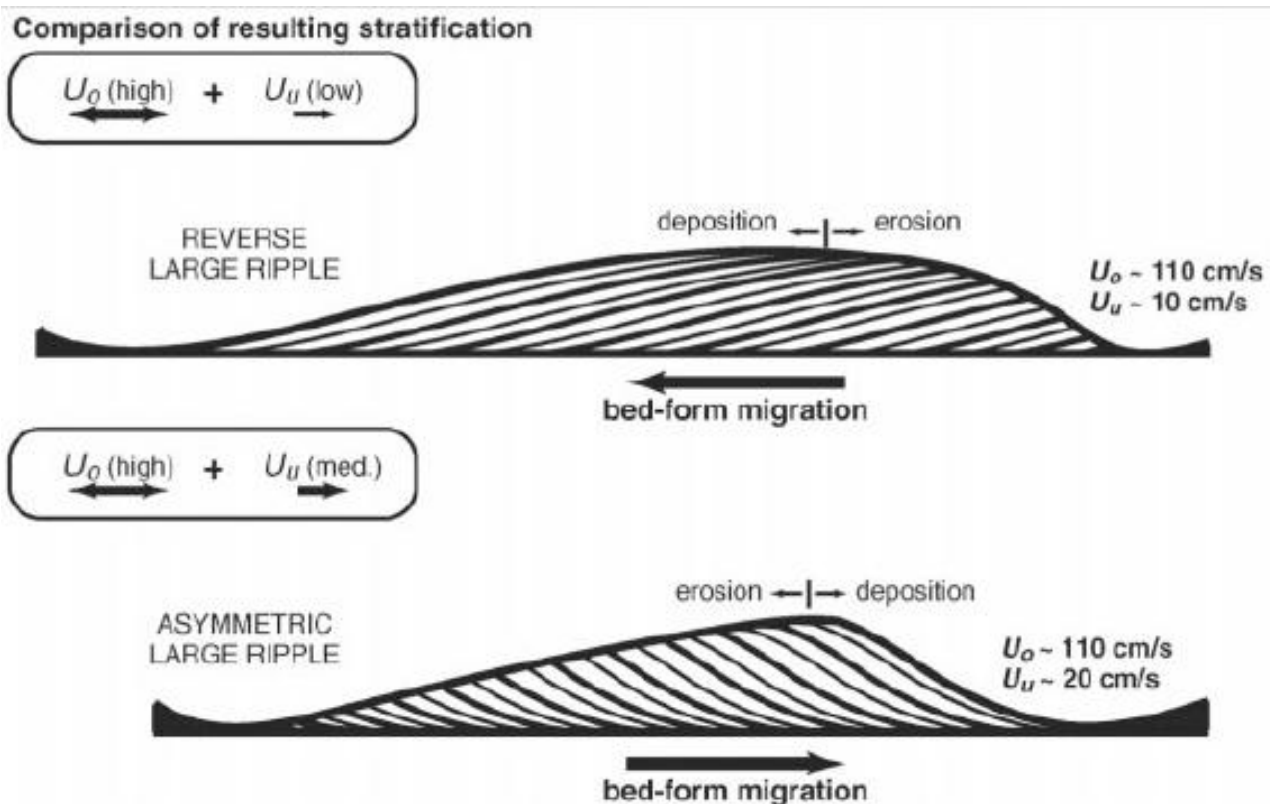


Figure 4. Sand fluxes and stratification a reverse large ripple. (1) Erosion and suspended sediment cloud at the lee side. (2) Suspension during the flow reversal. (3) Deposition downstream after the flow reversal. (4) Stratification of a reverse large ripple and an asymmetric large ripple (Dumas et al., 2005).

2.2 Ripple classification

In this chapter the model of *Clifton (1976)*, the classification of *Dumas et al. (2005)* and recent ripple predictions of *Goldstein et al., 2013* and *Nelson et al. 2013* will be discussed. Ripples can be subdivided into four fields (*Clifton, 1976*). For symmetric bedforms this still is a used classification, e.g. *Masselink et al. (2007)*. Laboratory experiments from *Dumas et al. (2005)* show a classification for bedforms under both unidirectional and oscillatory flow. With this classification also asymmetric ripples can be subdivided. The predictors of *Goldstein et al., 2013* and *Nelson et al. 2013* assume equilibrium conditions. There are no predictors available for non-equilibrium conditions.

2.2.1 The Classification of Clifton (1976)

The ripple classification of *Clifton (1976)* was used by *Masselink et al. (2007)*. The classical model of *Clifton (1976)* subdivides four main fields based on orbital velocity, velocity asymmetry, median grain size and wave period. The fields are namely: no sediment movement, symmetric bedforms, asymmetric bedforms and flat beds (*Figure 5*). The classification between these fields is based on the maximum velocity at the sea floor and the difference in maximum velocity at the sea floor between the crest and the trough. The boundaries of the fields are determined by the wave period and the grain diameter.

The model of *Clifton (1976)* made the following assumptions:

- Basic variables are combined in non-dimensional variables, assumed to be constant or left in dimensional form.
- The density (1 g/cm^3), kinematic viscosity ($0.01 \text{ cm}^2/\text{s}$) and sediment density (2.65 g/cm^3) are constant.
- There are only uniform waves.
- No unidirectional current exists.

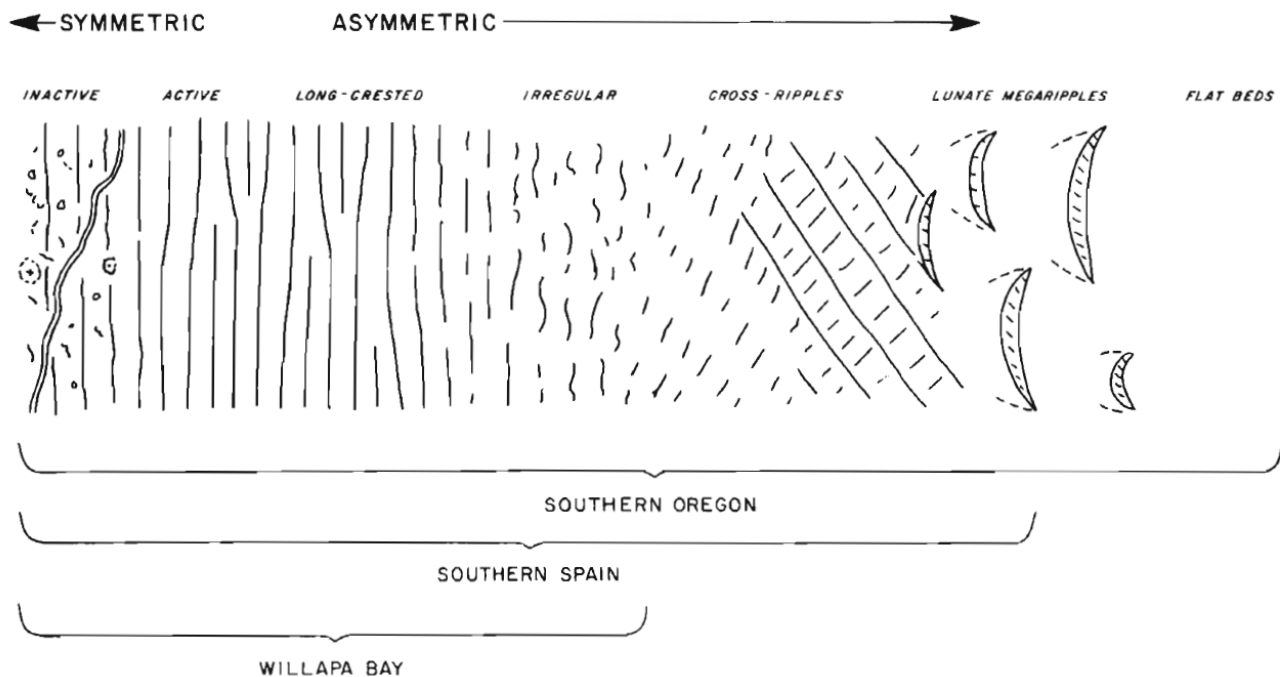


Figure 5. Classification of ripples, from left to right: no movement, symmetric bedforms, asymmetric bedforms and flat beds (*Clifton, 1976*).

From the four classified fields *Clifton (1976)* further subdivided the symmetric bedforms into orbital, suborbital and anorbital ripples. This sub classification is based on ripple wavelength and orbital velocity. The orbital ripples have a wavelength proportional to the orbital diameter, the anorbital ripples have a wavelength proportional to the sediment size and the suborbital ripples have an intermediate wavelength.

For this subdivision the ripple wavelength (λ) divided by the grain size diameter (D) vs. orbital diameter divided (d_0) by the grain size diameter is plotted (*Clifton 1976*). This plot is shown in Figure 5a. With the following formula's the diameter of orbital motion will be calculated. The wave number (k) is given by:

$$k = \frac{2\pi}{L} \quad (1)$$

Where L is the wavelength. Now the maximum velocity at the sea floor (u_m) can be calculated:

$$u_m = \frac{\pi H}{T \sin(h) k h} \quad (2)$$

Here H is the wave height, T is the wave period and h is the water depth. The diameter of orbital motion (d_0) is defined as:

$$d_0 = \frac{u_m T}{\pi} \quad (3)$$

The subdivision of the symmetric bedforms was used among others *Masselink et al. (2007)*. This article also uses another classification (Figure 6b): the ripple height instead of grain size is used. Hereby new terms are used: vortex and post-vortex ripples. The vortex ripples are sharp crested and have a steepness (η/λ) of 0.15, they develop under calm wave energy conditions. Post-vortex ripples are more rounded with steepness values ranging between 0-0.15 *Bagnold (1963)*.

Back to Figure 6a. Instead of using the *Clifton (1976)* model to classify ripples it is also possible to predict ripples. From laboratory measurements a prediction formula for orbital and anorbital ripples is found. The ripple wavelength of orbital and anorbital ripples can be predicted using the following formula's:

$$\lambda_{orb} = 0.62 \cdot d_0 \quad (4)$$

$$\lambda_{ano} \cong 535D \quad (5)$$

Here λ_{orb} is the wavelength of the orbital ripples, λ_{ano} is the wavelength of the anorbital ripples and D is the grain size diameter. For the subdivision between orbital ripples, anorbital ripples and suborbital ripples the diameter of orbital motion divided by the ripple height can be used. For more details see the article of *Wiberg and Harris (1994)*.

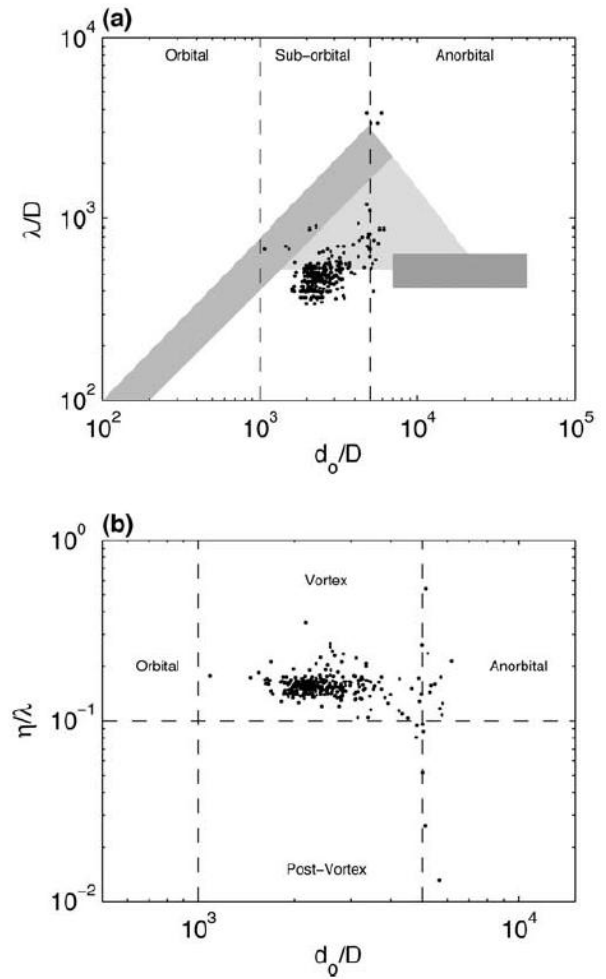


Figure 6. Two classification schemes used in (*Masselink et al., 2007*). λ =ripple wavelength, η =ripple height, d_0 =diameter of orbital motion, D =grain size diameter. (a) Classification of *Clifton (1976)*. (b) Classification with steepness values from *Bagnold (1963)*.

2.2.2 The Classification of Dumas 2005

From recent laboratorial experiments a bedform diagram for symmetric and asymmetric bedforms based on oscillatory and unidirectional flow velocities was made (Dumas et al. 2005). Clifton (1976) found no relation to subdivide asymmetric bedforms, like lunate megaripples. The classification, used by Clifton (1976), assumes that there is no unidirectional current. But in the surf zone unidirectional currents like an undertow, longshore currents or a rip current exist. When such a current is significant a classification based on only oscillatory flow can be questioned.

Laboratory experiments from Dumas et al. (2005) show a classification for bedforms under unidirectional and oscillatory flow. In Figure 7 a subdivision based on unidirectional velocity and oscillatory velocity is made. The bedforms are subdivided into: no movement, symmetric small ripples, asymmetric small ripples, symmetric large ripples, asymmetric large ripples, reverse large ripples, plane bed and hummocky 'zone'. The shape of the hummocky bedforms is similar to the lunate megaripples from Gallagher (2003). Depending on the grain size and the wave period the diagrams differ. The unidirectional and oscillatory flow is used to find a boundary between wave ripples and wave-current ripples. Values of the boundary are given by:

$$u_u/u_o < 0.55 \quad (6)$$

$$u_u/u_o > 0.55 \quad (7)$$

Here u_u is the unidirectional velocity and u_o is the oscillatory velocity. A ratio lower than 0.55 results in linear or irregular wave ripples while a ratio larger than 0.55 results in superimposed wave and current ripples (Larcy et al. 2007).

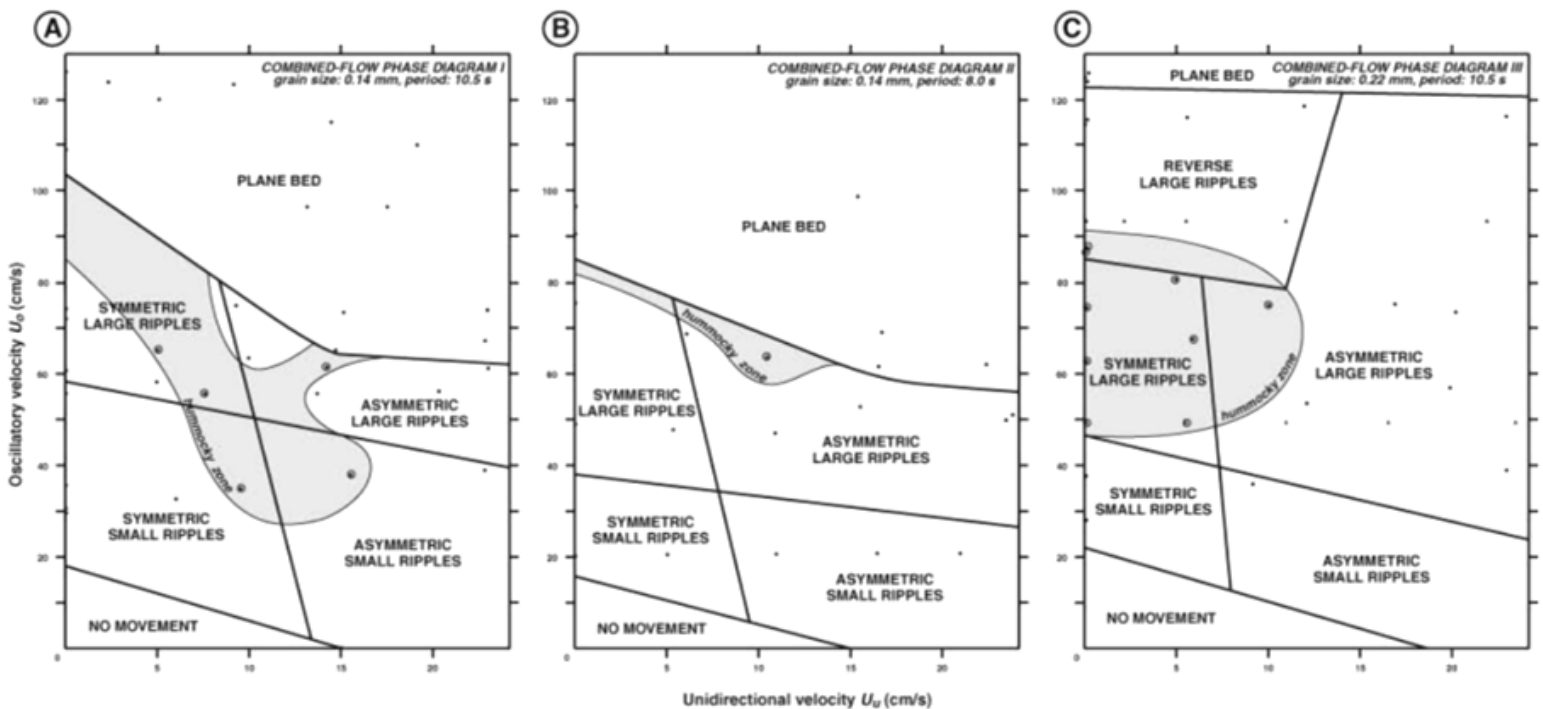
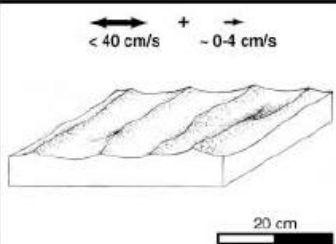
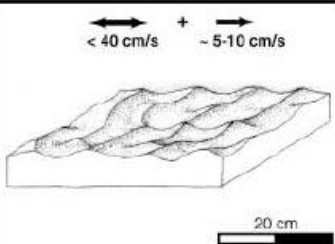
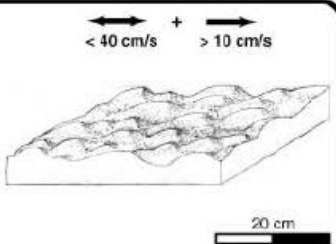
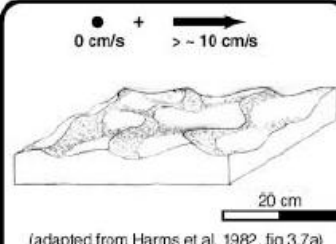
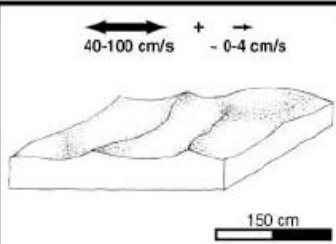
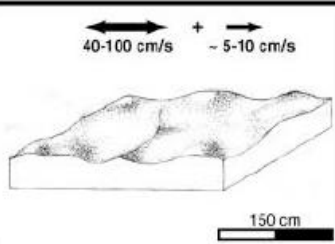
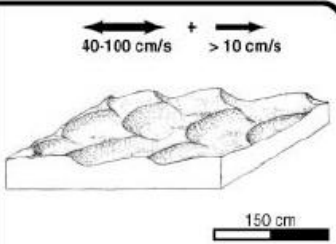
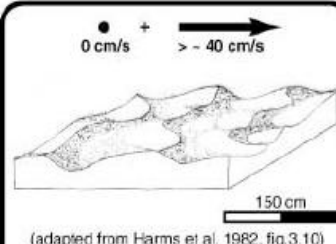


Figure 7. Bedform classification under oscillatory and unidirectional flow (Dumas et al. 2005). (A) $D=0.14\text{mm}$, $T=10.5\text{s}$. (B) $D=0.14\text{mm}$, $T=8.0\text{s}$. (C) $D=0.22\text{mm}$, $T=10.5\text{s}$.

In Figure 8 the characteristics of small-scale and large-scale bedforms is summarized. Notice that the classification has a gap between 20cm and 1m, there are thus no intermediate-size ripples. This suggests that the origin of small-scale and large-scale bedform is different. In other words a small-scale bedforms will not grow into a large-scale bedform. The ripple index (RI) has the same value for all bedforms (generally between 8 and 12), therefore RI is no use to differentiate between ripples. The symmetry index can be used to classify the large scale-ripples into symmetric and asymmetric bedforms (Dumas et al. 2005).

SMALL-SCALE BED FORMS: $\lambda < 20$ cm				
Bed form	Symmetric small ripples (SSR) regular, 2D, symmetrical, sharp crests, straight flanks, broad troughs	SSR + asymmetric small ripples (ASR) more irregular, 2-2.5D, still symmetrical rounder crests, some straight and some biconvex flanks	ASR + asymmetric large ripples irregular, 3D, asymmetrical, larger λ and height, round biconvex profiles, pronounced scour on lower end of stoss	Current ripples very irregular, 3D, sharp crests, steep and straight lee, convex-up stoss
Symmetry index	-1.2	-1.5		5-10 (Yokokawa 1995)
Dip of lee side	11-18°		*24-27° dip of lee side increases with increasing Uu	- angle of repose (30-35°)
Roundness index	0.44	-0.50	> 0.50	0.5-0.6 (Yokokawa 1995)
Ripple index	generally between 8-12 for all bed forms			12-22 (Harms 1969) 7-20 (Allen 1985a) 6-11, fsa (Yokokawa 1995) - 20, fsa (Boggs 2001)
Orbital diameter/wavelength	8-15	- 8-15	8-15	N/A
LARGE-SCALE BED FORMS: $\lambda > 100$ cm				
Bed form	Symmetric large ripples (SLR) SLR: 2.5D, symmetrical, sharp discontinuous crests = to brink, straight flanks	Hummocky (HM) + SLR + ALR HM: 3D, symmetrical, no brink point, broad round crests, domal, convex-up flanks	Asymmetric large ripples (ALR) ALR: 2D-3D, asymmetrical, brink not always = to crest, round stoss with break in slope, can have scour pits on lower end of stoss	Dunes regular (2D) to irregular (3D), sharp crests, steep and straight lee, straight to convex-up stoss
Symmetry index	-1.0 (≤ 1.5)	≤ 2	> 2	-
Dip of lee side	14-24° (SLR), 15-25° reverse large ripples (RLR)		*23-31° dip of lee side increases with increasing Uu	- angle of repose (30-35°)
Roundness index	-0.40-0.50 highest for HM bed forms	-0.45-0.60	-0.55-0.75 (up to 0.95)	-
Ripple index	generally between 8-12 for all bed forms			12-22 (Harms 1969) 20-40 (Allen 1985a) - 5, fsa (Boggs 2001)
Orbital diameter/wavelength	1-2	1-2	1-2	N/A

KEY: U_u , unidirectional velocity; λ , bed form wavelength; 2D, two-dimensional; 2.5D, locally 2D and locally 3D; 3D, three-dimensional; *, with the exception of one run; fsa, fine sand; N/A, not applicable
 NOTES: 1) oscillatory-flow and combined-flow data are compiled from the various conditions of grain size and oscillation period explored in this study. Unidirectional-flow data are generalized from the literature or specifically from cited sources.

Figure 8. Classification of small and large scale bedforms under combined and unidirectional flow conditions (Dumas et al. 2005).

2.2.3 Modern ripple predictions: Goldstein et al, 2013 and Nelson et al, 2013

Based on available datasets from both laboratory and field experiments a new equilibrium predictor for ripple length, height and steepness is introduced. The orbital ripples have a length proportional to the orbital diameter, the anorbital ripples have a length proportional to the sediment size and the suborbital ripples have an intermediate wavelength. In Figure 9 the bedforms formed by oscillatory flow are summarized. It is still unknown if suborbital and anorbital scale ripples exist for coarser grain settings (Goldstein et al., 2013). At the study side the grain size of $403\mu m$ is classified as medium sand, the boundary with coarse sand is $500\mu m$. Therefore it is possible that no suborbital and anorbital ripples are found.

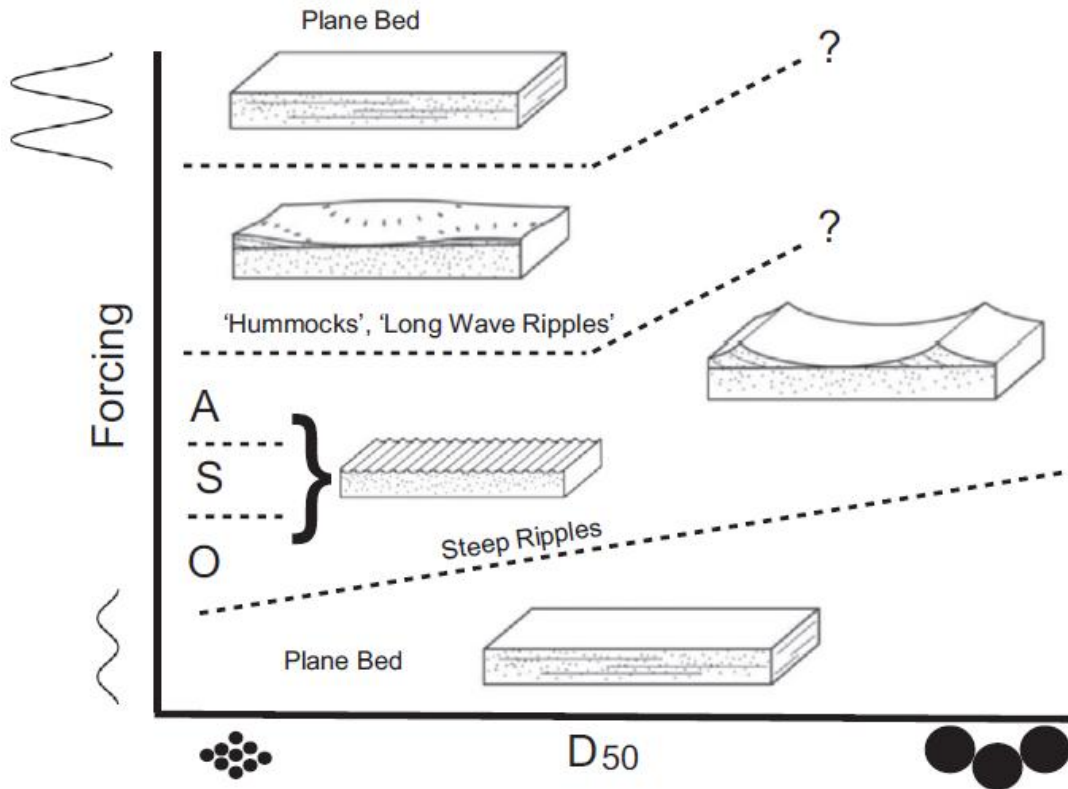


Figure 9. Schematic diagram for oscillatory flow bedforms (O=orbital, S=suborbital and A=anorbital ripples). Under calm hydrodynamic conditions orbital, suborbital and anorbital ripples are found. The boundary between plane bed and orbital ripples depends on the grainsize. Under stronger hydrodynamic conditions hummocks or long wave ripples are formed. The transitions are unclear and therefore denoted with a question mark (Goldstein et al., 2013).

Goldstein et al., 2013 compares different predictions, based on the SME (mean square error) the following formula is used to predict ripples length:

$$\lambda = \frac{d_0}{1.12 + 2.18(1000D)} \quad (8)$$

For the ripple height a similar analysis resulted in the following formula:

$$\eta = \frac{0.0237\lambda(1000D) + \lambda(1000D)^3 - 0.308\lambda(1000D)^2}{0.0332 + 4.46(1000D)^3 - 0.321D} \quad (9)$$

The ripple steepness (θ) can now be predicted:

$$\vartheta = \frac{3.42}{22 + \left(\left(\frac{\lambda}{1000D}\right)\right)^2} \quad (10)$$

These predictors, for ripple length, height and steepness, are suitable for conditions with no significant currents. Notice that they are non-linear functions.

Nelson et al., 2013 provides predictions for regular (from laboratory measurements) and irregular waves (from field measurements). For regular waves the following prediction is found:

$$\lambda = 6.76A_{b13}^{0.68}D^{0.32} \quad (11)$$

Here the orbital semi excursion is the dominant parameter for the ripple length. This is different for irregular waves:

$$\lambda = 2.22 * 10^3 \cdot A_{b13}^{-0.11}D^{1.11} \quad (12)$$

The dominant parameter controlling the ripple length here is the grain size. Although these formula's for regular and irregular waves are different it was found that the ripple steepness is relatively constant for both conditions. For the irregular waves the prediction for ripple length is as following (*Nelson et al., 2013*):

$$\eta = 0.126 * \lambda^{1.05} \quad (13)$$

Both predictors, *Goldstein et al., 2013* and *Nelson et al., 2013*, assume equilibrium ripple conditions. For the constantly changing hydrodynamic conditions of the intertidal area, at the study site, this might not be the case.

2.2.4 Classification of co-existing ripples

Different ripple structures can co-exist. An example is co-existing megaripples and wave ripples (Miles, 2013) or co-existing wave and current ripples (Blondeaux, 2000). A ripple field containing two ripple types cannot be classified like in Figure 8, because it can be classified as two ripples at the same time.

During the experiments from Blondeaux, (2000) length, height and symmetry index were measured (see Figure 2 for the terms). Ripple formation under sea waves is analysed with the momentum equation, they found that their dimensionless parameters control the ripple characteristics (such as wavelength).

For the classification of megaripples and wave ripples a solution is presented in Miles (2013). Each line scan of the sea bed was decomposed into a wave ripple component ($\lambda < 35$ cm) and a megaripple component ($\lambda > 35$ cm) using a frequency domain filter (Figure 10). The wave ripples and megaripples can be analysed separately. This method is useful analysing the sonar images.

The disadvantage of a 2D line scan is that the direction of the scan influences the estimated wavelength of the ripples. If for example the angle of the line scan would be in the same direction as the crest of a wave ripple, this wave ripple would not be recognized.

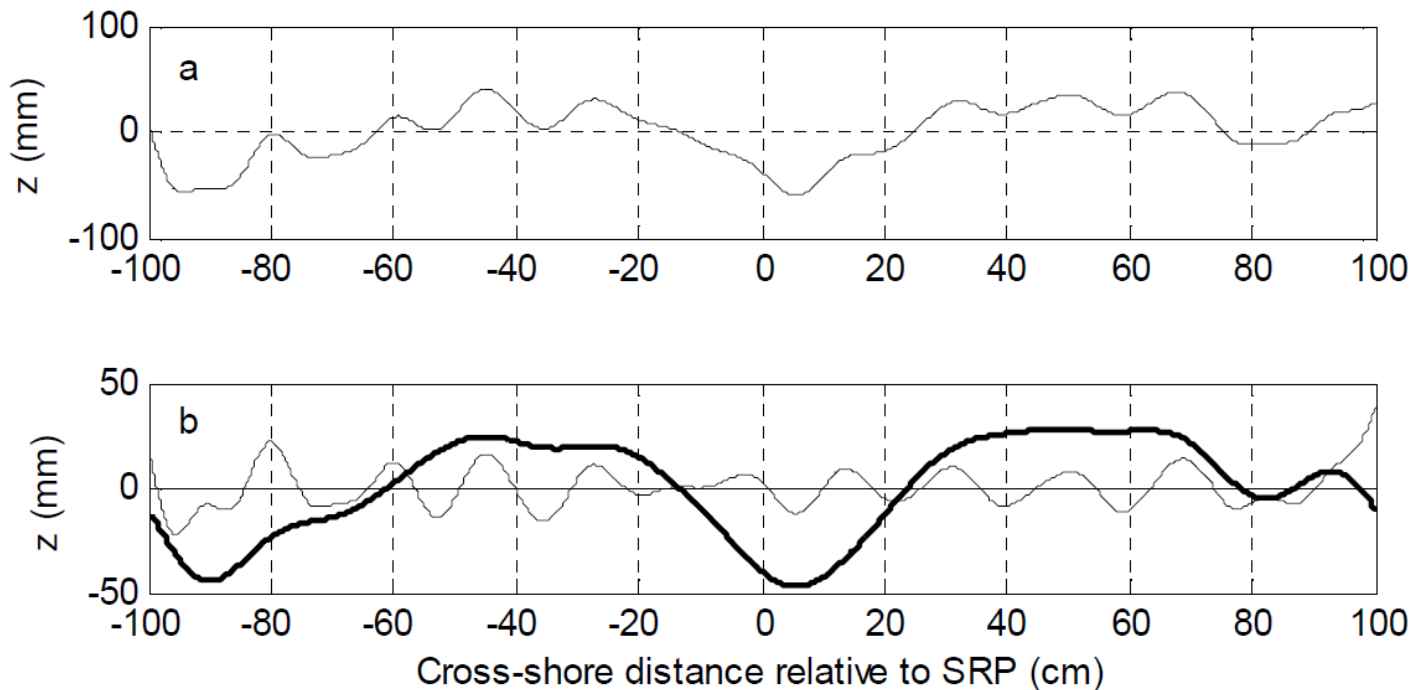


Figure 10. 2D line scan of the sea bed (Blondeaux, 2000) .(a) Measured bed elevation. (b) Filtered bed elevation for low frequency and high frequency ripples.

3. Problem definition and research questions & aims

Hydrodynamics are highly variable in the intertidal zone, within a time span of 6 hours, the swash zone changes into a location with breaking waves, shoaling waves and vice versa. Moreover, waves and currents in the nearshore are in general also highly variable. Due to this variability, relatively little is known about ripple dynamics in the intertidal zone. Field measurements of waves, currents and bedforms show that the relaxation time of the ripple formation depends on rising or falling tide. While during rising tide an equilibrium is quickly reached, during falling tide this is not the case. During falling tide, the hydrodynamic conditions change at a fast rate compared to the relaxation time. This implies that equilibrium predictors may perform adequate during rising and high tide, but fail during falling and low tide (Austin et al, 2007). Bedform characteristics can be highly variable in the intertidal zone. Large spatial, cross and longshore, variations in ripples were found by Thornton et al. (1998). They linked the cross shore variation to changing waves and induced currents, but the longshore variability is left unexplained. *Clifton (1976)* provides one of the first classification for orbital, suborbital and anorbital ripples. Equilibrium predictors for ripple length, height and steepness are available, e.g. Goldstein et al, 2013 and Nelson et al, 2013. Can these models provide a classification for the ripples in the intertidal area? More field data is needed for a proper understanding of ripple variability, relaxation time, equilibrium conditions and the applicability of classification methods. This thesis will focus on ripples in the intertidal zone of a natural beach, and their relation to the hydrodynamics. The main goal of this study is:

To explore methods to quantify the 2D and 3D characteristics of ripples in the intertidal zone and relate these characteristics to hydrodynamic conditions.

To reach the main goal several sub questions will be answered:

- How can ripple characteristics be quantified in an objective way?
- What kind of ripples can be found in the intertidal zone?
- Is there a relation between ripple length, height, orientation, and the hydrodynamics?
- How can ripple regularity be classified in an objective and quantitative way?

4. Methods

4.1. Data Collection

The data for this study was collected in the Fall of 2014, during a 6 week fieldwork, as part of the MegaPex14 campaign. During this campaign, data on hydrodynamics, morphodynamics, hydrology, aeolian processes and ecology was collected. This fieldwork was conducted at the Sand Motor, a man-made peninsula of 1 km² at the Delfland Coast, the Netherlands (Figure 11A). The Utrecht Coastal Group investigated an array from low water level to above high water level. The study site was located at the southern side of the Sand Motor (Figure 11B). For this study, data was collected in the intertidal zone. The beach was north-south oriented and had a slope of approximately 1:30. The median grain size was 400 μ m, based on samples. The measurement campaign was mainly during calm weather conditions, with small wave heights, but occasionally the wave height exceeded 1m in the intertidal zone (Figure 14a). The waves arrived between 50° and -50°. The tide is classified as 'mixed, dominantly semi-diurnal'. During neap tide, tidal variations are 1.5m or less, during spring tide around 2m.

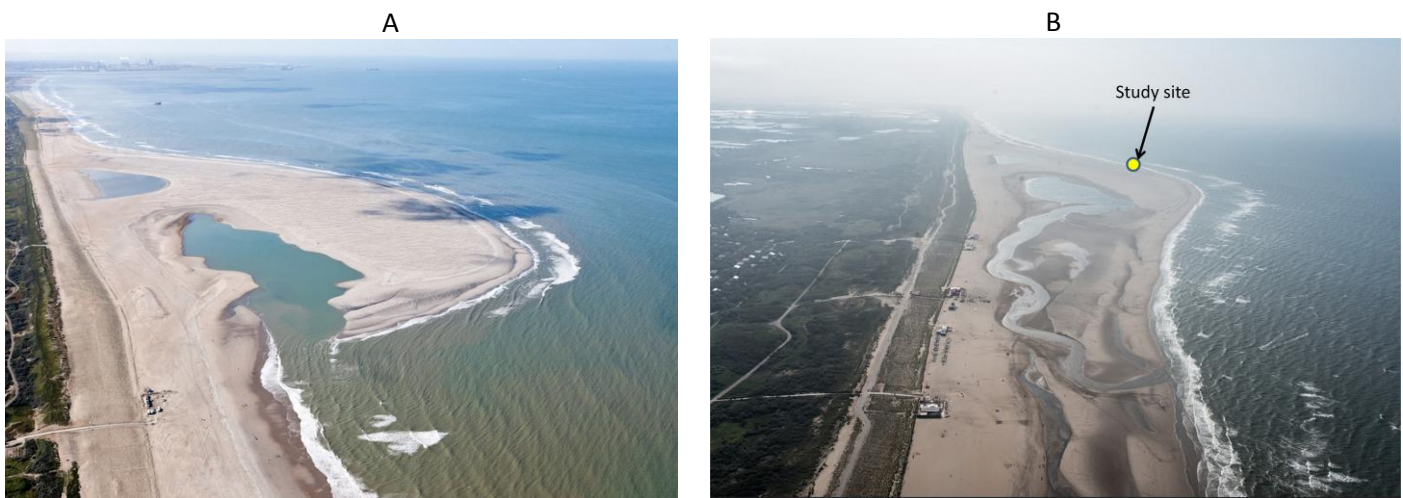


Figure 11. Evolution of the Sand Engine. (A) The Sand Engine at October 2011. (B) The Sand Engine at September 2014. The yellow dot indicates the location of our measurement array (www.dezandmotor.nl).

Figure 12 shows the cross-shore location of the rig. During the fieldwork the beach profile was measured every day with a DGPS (Differential Global Positioning System). Figure 13A represents two typical transects of the intertidal area of the study site (20 September and 14 October). The intertidal bar and the berm, present during the in the first weeks of the measurement, are absent at 14 October. From a longshore bar-trough beach the profile changed into a more dissipative beach.

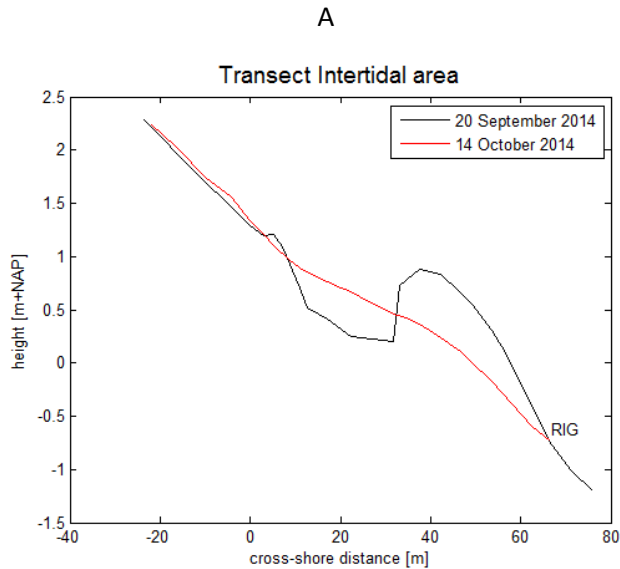


Figure 12. Beach profile of the intertidal area. (A) Two transects, measured with DGPS, including the position of the rig (location of the sonar). Notice that a bar is present at 20 September but absent on 14 October. (B) Visualisation of the measurement location and the transect on 20 September, from land to sea.

In Figure 13 an overview of the rig is presented. The rig was deployed near the low water line, so the rig was accessible to retrieve data and check functionality every day during low tide. The height of the instruments above the bed was measured every day. The data from the rig was retrieved every three days. To this rig the following measurement devices were attached: 3 ADV's, 1 EMF, 7 OBS's, a sonar and a pressure sensor. All instruments were placed so that the disturbance of the frame on the measurements was minimum. The frame's orientation was south-west, as waves were expected to arrive mainly from this direction. The height of the instrument above the bed varied during the measurement period, mainly due to erosion. The pressure sensor and float switch were attached to the landward pole. The pressure sensor had an initial height of 9.5cm above the bed, and measured at a frequency of 4 Hz. The water depth, wave height and period were derived from the pressure data. The EMF (Electromagnetic Flowmeter) measured cross-shore and longshore flow velocity with a frequency of 4Hz. The initial height of the EMF was 25cm above the bed. The bedforms were measured with a 3D sonar, scanning the bottom every 15 minutes during high water. A scan takes approximately five minutes and is composed of 200 2D slices, each separated by an angle of 0.9 degrees and thus covering a full circle.



Figure 13. An overview of the rig in the field. The sonar was attached at the seaward side of the frame, like the other instruments. Here the measurements were least disturbed by the frame.

During the fieldwork several difficulties were encountered. Due to erosion, the frame tilted, resulting in a constantly changing angle of the instruments. This affected the hydrodynamic data, e.g. the longshore and cross-shore measurements as well as the apparent angle of incidence of the waves. Also the orientation of the sonar changed over the measurement period. To compensate for the frame tilt, a correction for the orientation of the instruments was made regularly. Once the frame topped over due to erosion, clearly the data of this period was not used for analysis.

Figure 14 provides an overview of the hydrodynamic conditions during the field campaign, the following parameters are shown: high frequency wave height, peak period, wave angle, cross shore velocity and longshore velocity. The sonar data was collected under a large variety of wave heights, periods, angles and velocities. Based on the hydrodynamic conditions it is expected that the ripple data also shows this large variety. When the high frequency wave height (Figure 14a) exceeds 0.8m there was no sonar data collected.

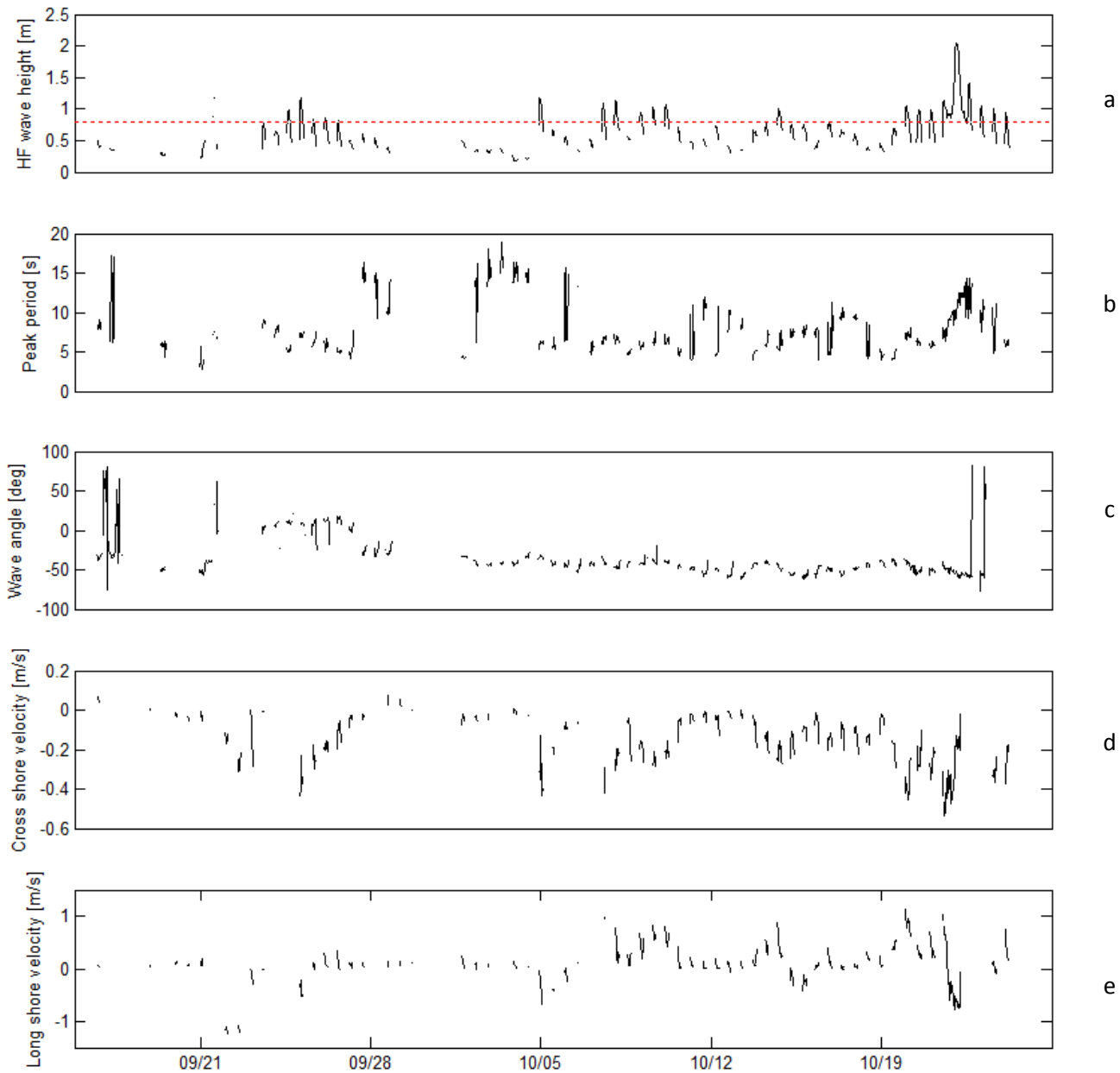


Figure 14. Overview of the hydrodynamic conditions during the field campaign. Except for the velocities, all parameters from this figure were measured by the rig. The velocity measurements are from Mini13, 20m shoreward of the sonar rig (a) High frequency wave height, with an average of 0.64m, during a storm wave heights above 2m were observed. The red dotted line indicates the maximum wave height when ripples were measured. (b) Peak period, on average 8 seconds, with a standard deviation of 3.3 seconds. (c) Wave angle, on average the waves arrived -36° N, with a standard deviation of 24° . (d) Cross shore velocity, with positive velocity landwards, from Mini13, on average -0.15m/s , with a standard deviation of 0.13m/s . (e) Longshore velocity, with positive velocity towards the North, from Mini13, on average 0.09m/s , with a standard deviation of 0.39m/s . Notice the high offshore velocities during the storm (with a maximum of -0.78m/s).

4.2. Data Processing

4.2.1 Two dimensional ripple images: Line scans

The sonar transmits an ultrasound wave towards the sea bottom and receives the reflected sound waves. A sound wave reflects at an interfaces when the so-called acoustical impedance, i.e. the product of sound speed and density, deviates from the acoustical impedance of sea water. A so-called 'time of flight' measurement, involving the speed of sound, is used to calculate the water depth. The reflections with the highest intensity occur at the water - sea floor interface. In Figure 15 an example of a 2D scan is shown, where the detected sea floor is indicated by the black stars. Directly under the head of the sonar, the image has a better resolution compared to the edges of the image. At the edges of the image the data quality is less due to a ripple shadow effect and the increased distance. The unfavourable angle of incidence of the sound waves and increased sampling distance influences the data quality.

The raw sonar data is converted to a line scans (2D) of the sea bottom (Figure 15). The bottom is characterized by a high intensity reflection, which is detected.

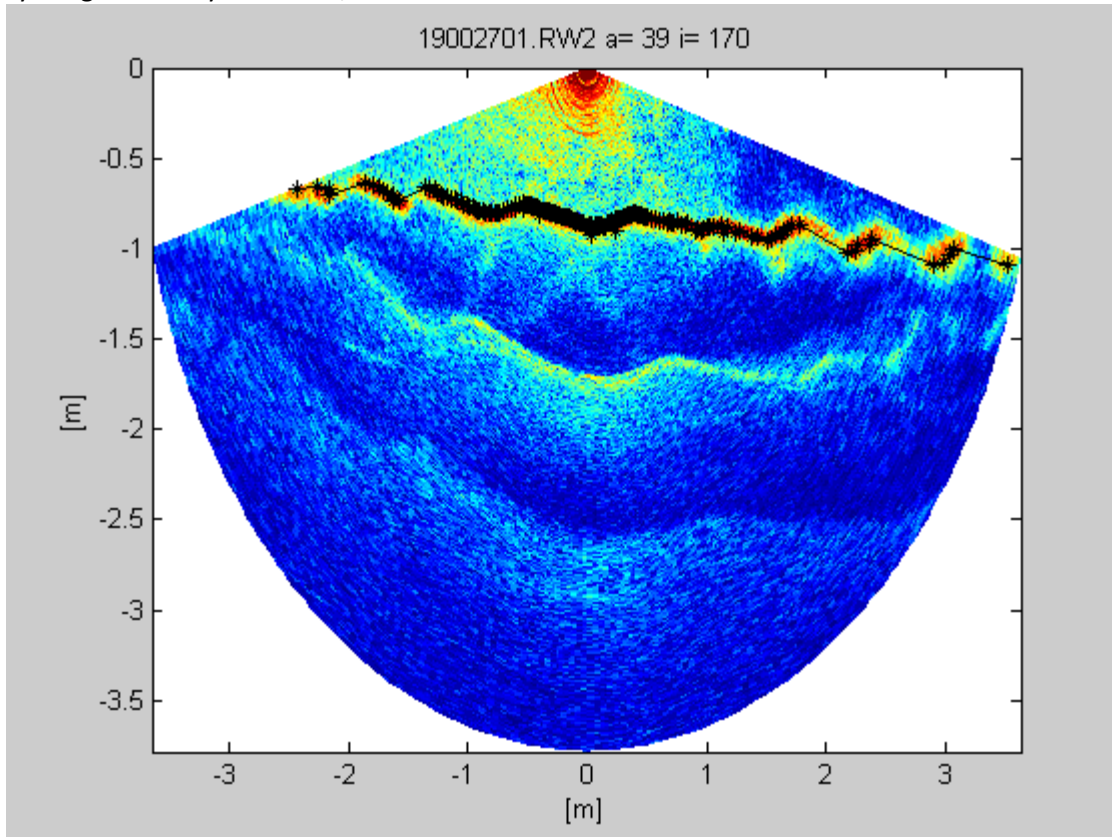


Figure 15. An example of the raw sonar data is shown (".RW2" file). Superimposed (the black line) indicates the sea bottom. The head of the sonar is at [0,0].

The high intensity close to the sonar head, indicated in Figure 15 by the red spot at [0,0], is a measurement artefact and excluded from the measurement by setting proper boundaries. Additional structures show up in the sonar image, these are reflections between the bed and the water surface. In order to detect the seabed, a minimum level was set to 0.6m below the sonar head and the maximum values was set to 1.2m below the sonar head. For some datasets these values were adjusted as the height of the sonar above the seabed was not constant throughout the entire measurement period.

4.2.2 Sonar Images in 3D

3D sonar images are compiled from 2D cross sections. The sonar head rotates over 180 degrees from an eastern to western direction within 5 minutes. Within this time the 200 line scans were recorded. These line scans were combined into a 3D-seabed on a regular grid. The sonar captures a 3D-seabed profile every 15 minutes. An example of a 3D image is shown in Figure 16 (A). Due to the scan rotation, a circular area with a radius of approximately 3m was obtained. The

quadratic loess interpolation method was applied to convert these data to a regular grid. This interpolation method is controlled by the parameters λ_x and λ_y , of which the value controls the distance to observations used for an estimate. The appropriate value for these parameters depends on the measurement resolution and the shortest scale of interest (Plant et al., 2002) as:

$$4\Delta x < \lambda_x < 0.5L_0 \quad (15)$$

Here Δx is the distance between the data points and L_0 is the shortest scale of interest (Plant et al., 2002). The shortest scale of interest of the sonar data is estimated at 0.3m, corresponding with $\lambda_x=0.15m$. Each line scan contains 166 data points, over a distance around 6m. From this the average distribution of the points on one line scan is found to be: $\Delta r = 3.6cm$ (or $\lambda_x=0.14m$). Thus, according to equation 15 the optimal value for $\lambda_x=0.15m$.

The sonar scans at a constant angular interval. Consequently the data points are distributed on a non regular grid, with increased spacing between the data point for an increasing radial distance. At the edges of the image, with a radius of $R = 3m$, the distance between the points is found to be: $R\Delta\theta = 5cm$.

The reconstruction of the image fails when $\Delta R > \lambda_x$. For small values of λ_x the area of the reconstructed image decreases. This effect is pronounced for $\lambda_x < 0.2$. Therefore, the value is $\lambda_x = 0.2m$, is used for the analysis, close to the value used by Plant et al., 2002.

To remove the bed slope and the tilting of the sonar, the convenient algorithm used for de-trending the entire image was:

$$a + bx + cy + dx^2 + exy + fy^2 \quad (16)$$

Where $a + bx + cy$ is the linear correction and $dx^2 + exy + fy^2$ is the parabolic correction. The linear correction is much larger than the parabolic correction. With a linear correction the root mean square (RMS) was 450mm with a maximum value of 1200mm. The maximum parabolic correction at the edge of the images, was typically less than 10mm, but in the centre much smaller. The RMS correction of the entire dataset was less than 5mm. Features that were filter with this correction are large scale sand bar slopes.

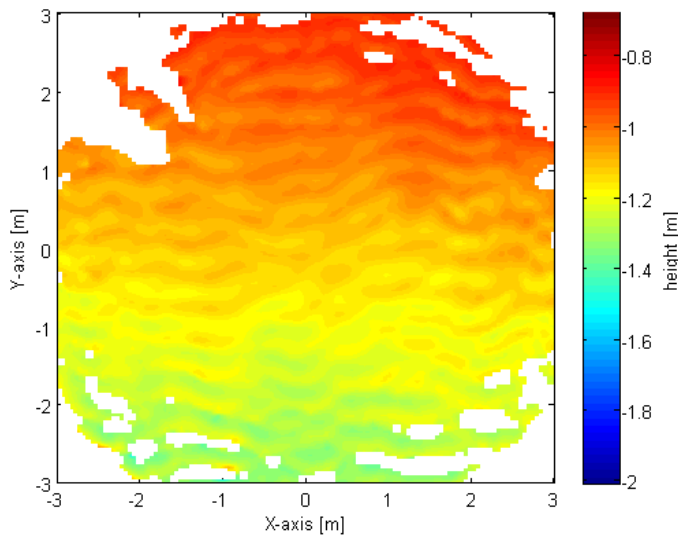


Figure 16. Reconstructed 3D sea bottom from the line scans, where the Loess filter has been applied. The data is interpolated on a regular grid, but no de-trend was applied yet. White area's correspond to NAN values, where reconstruction was not possible.

For each image the number of NAN's was recorded. The fraction of valid data points (Q) of the 3D image resembles the number of NAN's present in a image: the fewer NAN's the higher Q. This number helps to select the proper data, which is mostly collected during high tide. Figure 17A shows Q over a time span of 6 hours. At first Q increased to a maximum value of 80%, 3.5 hours later Q drops.

Q is strongly correlated to the water depth (Figure 17B), as the sonar has to be fully submerged to collect useful measurements. When the water depth was higher than approximately one meter Q increased. Also the wave height played an important role. If the waves were too high (~0.8m), the sonar did not measure.

In addition suspended sediment, air bubbles or parts of the rig disturbed the image, causing outlier. To remove these outliers a filter was applied: for every 20 by 20 cm outliers were filtered. The median of each window was calculated and every point deviating more than 7cm from this median was excluded from the data analysis.

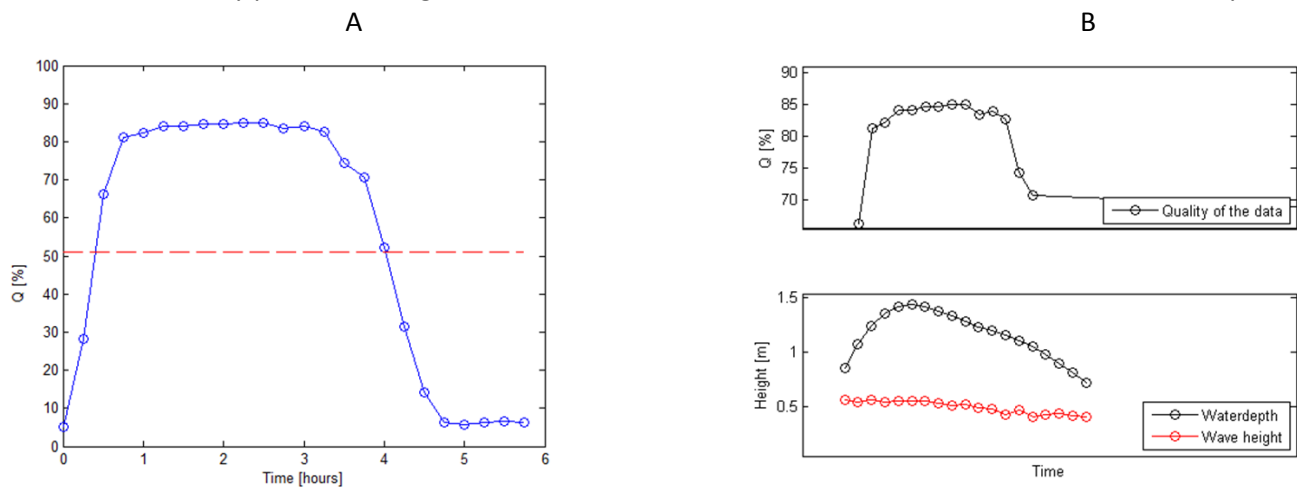


Figure 17. The fraction of valid data points (Q) of the interpolated 3D sonar images. Q is given in a percentage for each 3D image, values above 50% are selected, as indicated by the red dashed line (A). Relation between the data quality, waves and water depth. When the water depth increases the data quality also increases (B).

4.2.3 Hydrodynamic data

The pressure sensor was a pressure transducer. The raw pressure signal was corrected, with the atmospheric pressure, measured close to the field site, to obtain the water height (m). The sea surface elevation was calculated using linear wave theory (Ruessink, 2010).

The correction for the EMF converts the raw velocity signal (mV) into velocity data (m/s). The first step in converting the raw velocity is selecting the submerged data, based on the amplitude of the backscatter signal. Next, the beam velocities with low correlations were rejected, others were interpolated. The beam velocities were then transformed into an orthogonal coordinate system, with cross shore and longshore velocities (Ruessink, 2010). Positive cross shore velocity (u) was landwards and positive longshore velocity (v) had a northern direction. The data is despiked using the Mori method (Mori et al., 2007). Finally, there has been a correction for the orientation of the EMF, based on the orientation measurements (measured approximately every 2 weeks).

4.3. Data Analysis

4.3.1 Ripple characteristics

The goal of the analysis is to characterize an in general irregular ripples pattern from each 3D image with several parameters. The Ripple height (RMS value), i.e. estimated from the $\sigma * 2\sqrt{2}$ standard deviation of the ripple height distribution. Ripple wavelength. The ripple wavelength and orientation were calculated using a Fourier analysis. Complicated patterns are characterised by a distribution of angles and wavelengths. The Rotational diagram method is used to calculate the ripple regularity index.

4.3.2 Fourier analysis: the basics

In contrast to *Nelson & Voulgaris (2014)* the Fourier analysis on the 3D image was conducted on the entire image. Hereby larger ripple structures, like megaripples, can also be recognised. The second advantage was that the Fourier analysis uses only one window, in short: at the edges of the analysed image values smoothly approach zero. How the window goes to zero depends on the chosen method. So if you have a small image the window may affect your results. Here the window was defined as:

$$Window = \exp\left(-\frac{(X^2 + Y^2)^2}{r^4}\right) \quad (17)$$

The spatial domain is X,Y with a radius r. The Fourier expansion relates the spatial domain (x,y) to the frequency domain (p_x, p_y). Thus a Fourier expansion of the seabed represents the ripple periodicity and orientation. For simplicity the definition of a 1D Fourier series is given below. For each function f(x) defined in the interval (-L,L), and determined outside of this interval by $f(x+2L)=f(x)$. It is assumed that f(x) has the period 2L. The 1D Fourier series of f(x) is defined as:

$$f(x) = \frac{a_0}{2} + \sum_{n=1}^{\infty} a_n \cos\left(\frac{n\pi x}{L}\right) + b_n \sin\left(\frac{n\pi x}{L}\right) \quad (18)$$

$n\pi/L$ are the periods that occur in the Fourier domain (Spiegel, 1974). The Fourier coefficients a_n and b_n are calculated in a numerical way. For the seabed evaluation the Matlab built-in discrete 2D Fourier transform was used. So the de-trended and filtered data were further analysed using a Fourier analysis. Ripple periods and angles were derived from a Fourier analysis.

Figure 18A shows the 2D Fourier transform of the seabed. Note that distinct and clear maxima are obtained, representing a specific wavelength and angle of the ripple structure. Figure 18B shows a typical 3D seabed with the dominant ripple orientation (line), 2x the dominant period indicated (solid circle) and the window (dashed circle).

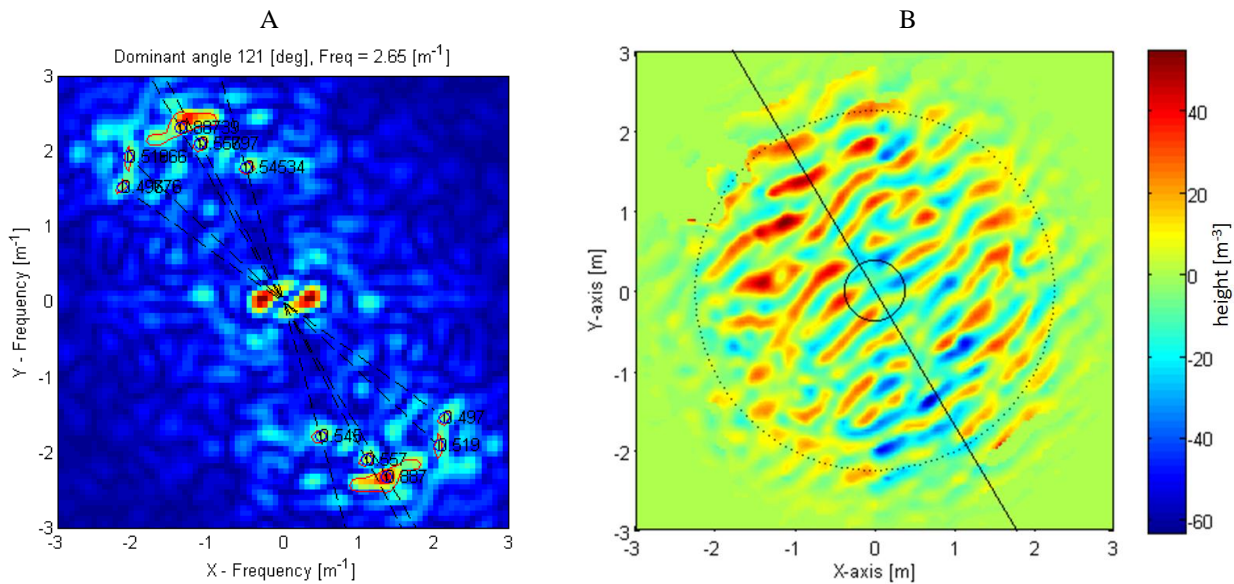


Figure 18. Fourier analysis of the 3D surface. (A) The Fourier transform. Notice that the peaks in the Fourier spectrum appear in pairs. The wavelength equals the distance from a peak to the center. Note that there are distinct peaks and not a continuous distribution, which can be described with for example a power density function. The contour analysis detects these different peaks and analysis them individually. (B) An example of a 3D surface, with a height of 37,8 mm.

A contour algorithm detected the local maxima, the maximum with the highest amplitude represents the dominant wavelength and angle of the ripple pattern. In this example, a total of five peaks were detected (Figure 18B). The amplitude weighted average of wavelength and angle represent the ripple angle and average period. Matlab organises the contour plot in a single vector (Figure 18A). The first step in the contour algorithm is to identify individual contours, where each contour was characterized by location and intensity. For convenience, a structure was used to organize the contours, and to store their properties such as the centre position, contour coordinates, distance from the origin and contour level. These properties were used to filter and select contours. Only closed contours were selected for analysis. As the Fourier analysis always has a 'positive' and 'negative' frequency, by definition, the contours appear in pairs, those were used to calculate the orientation (angles).

First, contour levels were defined in the range of 0.1 to 0.9. Prior to filtering, typically 200-600 contours are found for each image. For each contour the average frequency was calculated. Figure 19 shows the frequency histogram of the entire data collection. It appears that two regions can be distinguished, as indicated by the red dashed line: a high frequency range (more than 1 per meter) and a low frequency range (less than 1 per meter). The high frequency (HF) range associated with small scale bedforms and the low frequency (LF) range are associated with large scale bedforms. Wavelength of 5m or more could not be detected, as the image size was insufficient. The idea of using a frequency filter was first used by *Miles et al. (2003)*. Each image was decomposed into a wave ripple component ($\lambda < 35$ cm) and a megaripple component ($\lambda > 35$ cm) using a frequency domain filter.

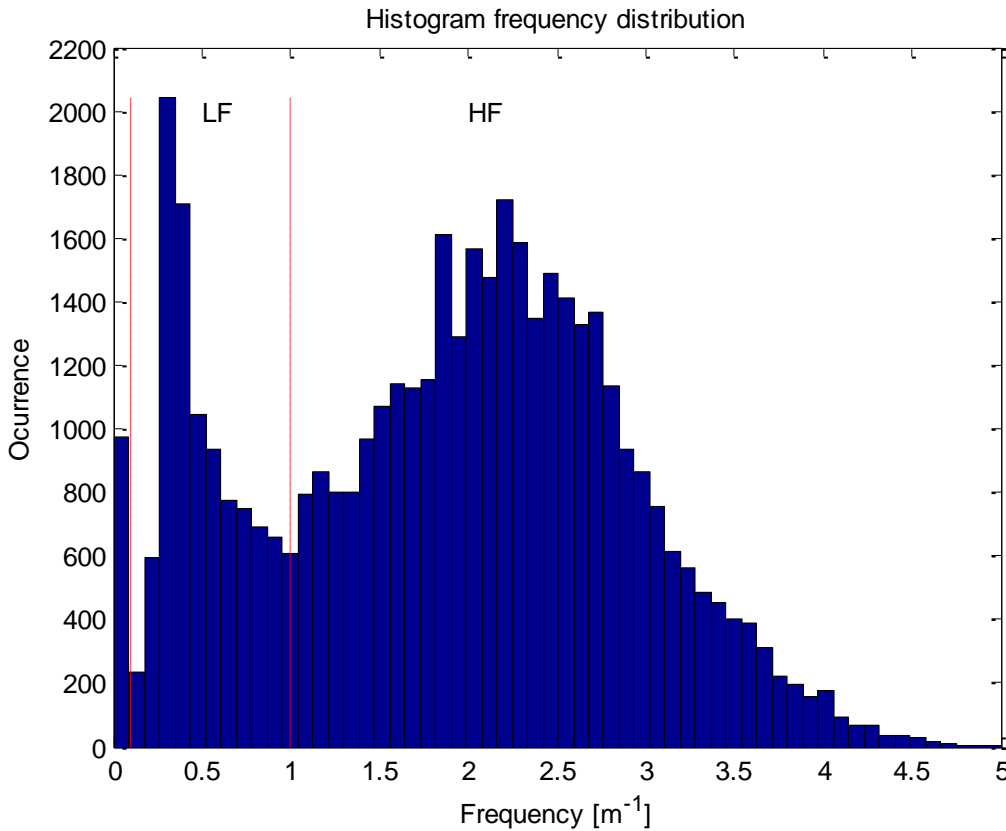


Figure 19. Frequency histogram of the entire dataset. Two frequency domains were distinguished: low frequency (LF) and high frequency (HF). Especially HF data was used for further analysis.

4.3.3 Effect of the Loess filter settings on the Ripple Amplitude

The calculated height of the 3D sonar images depends on the settings of the Loess filter, in particular on the value of λ_x , λ_y . Here the value of λ_x and λ_y were equal. The value of λ_x , λ_y is a tradeoff between quantity and quality of the data. Small values result in smaller usable image size while a large value underestimates the actual height of small periods. The dataset of 11 October was selected to explore the effect these parameters on estimated ripple height. This dataset contains two tidal period with various ripple periods, representing the entire dataset. The settings for λ_x ranged from 0.05 up to 0.25. Although the analysis in this report used the setting $\lambda_x = 0.2$, the value of $\lambda_x = 0.1$ is more appropriate for the height detection of small periods. To correct for this, a correction factor as a function of the average period was calculated (Figure 20). The correction factor (reference height by $\lambda_x = 0.1$ divided by the height estimated by $\lambda_x = 0.2$) is a function of the period (which is not altered significantly by the changes in λ_x). The height of $\lambda_x = 0.1$ was comparing with the raw data and found to be representative for the actual height.

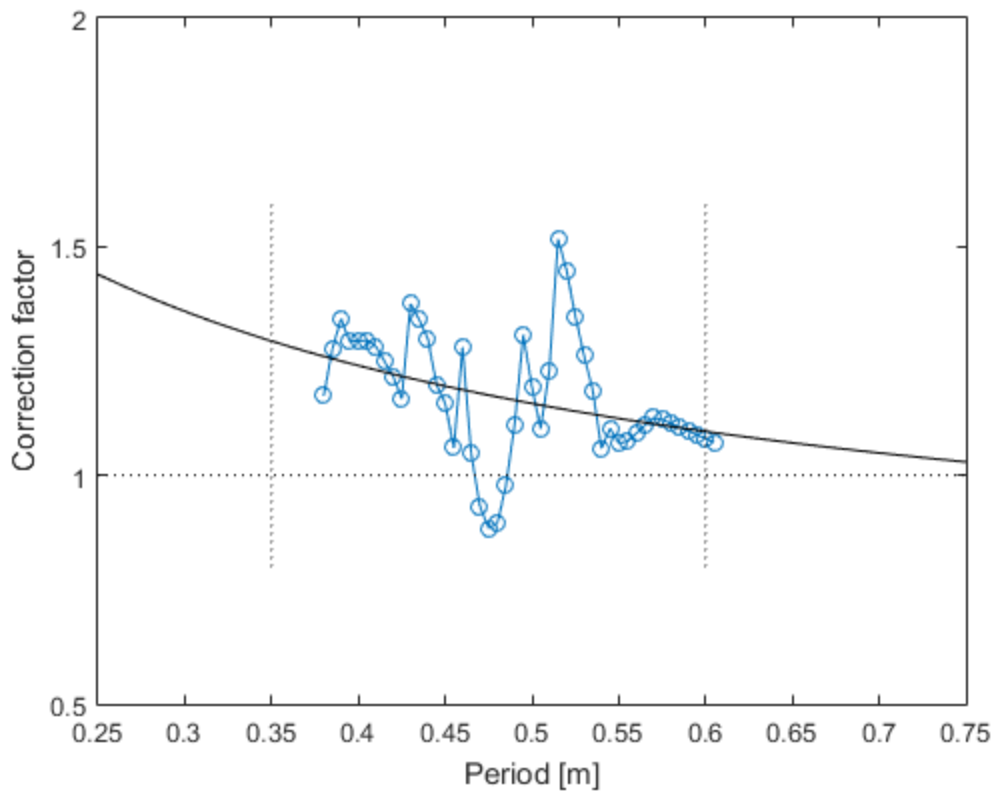


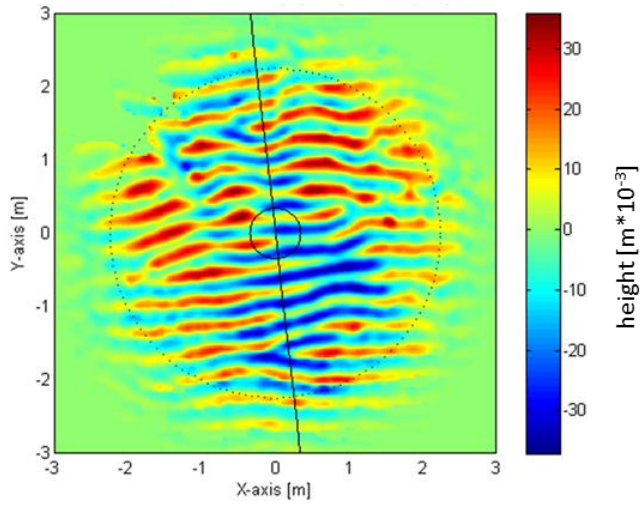
Figure 20. Estimate of the RMS height correction factor as a function of the average period, for $\lambda x = 0.20$, taking the case of $\lambda x = 0.1$ as reference. The RMS value of the correction factor equals 0.13, for the smallest ripple periods (0.35m) the correction factor is about 1.3. For larger periods the corrector factor approaches 1.

4.3.4 Examples of the dataset

Large variation in ripple characteristics was observed. The ripple pattern varied within tides and between the tides. Various examples are presented in Figure 21. Figure 21A shows a regular ripple pattern of small scale ripples with bifurcating crests, that were also found for the irregular, larger, ripple pattern of Figure 21B. Besides these relatively small ripples also larger ripples, of 0.8m or more, were observed (Figure 21C).

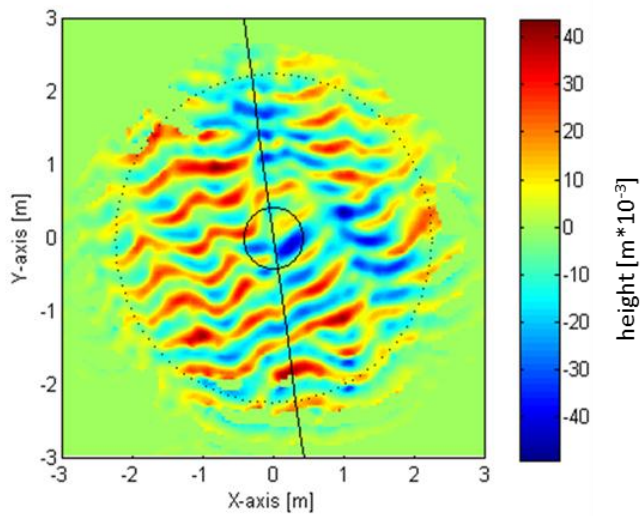
Figure 21. Three examples of 3D ripple images and their characteristics. An angle of 0 degree corresponds with the North. An angle of 90 degrees implies ripples perpendicular to the shore, this angle is characteristic for wave ripples. The dominant angle and length are indicated by respectively a line and a circle. The average angle and length may deviate from the dominant angle and length as several lengths and angles are found for each sonar image. The amplitude of the ripples was estimated from a *standard deviation* of the sonar image. For further analysis average angle, length and height were used. Various ripple shapes were found: (A) Regular ripple pattern with small scale ripples. (B) Irregular ripples, larger than in (A). (C) Large irregular ripple structures.

A



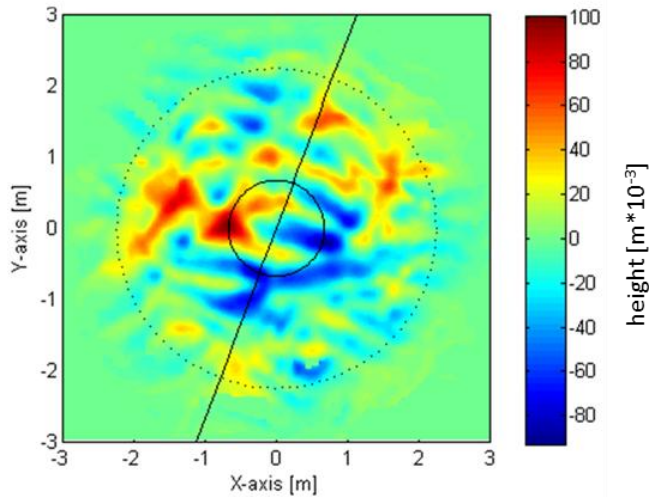
Date	01-Oct-2014
Average orientation	94.4 degree
Average length	0.36 m
Amplitude	$20.1 \cdot 10^{-3}$ m

B



Date	27-Sep-2014
Average angle	104.3 degree
Average length	0.44 m
Amplitude	$20.6 \cdot 10^{-3}$ m

C



Date	17-Oct-2014
Average angle	85.6 degree
Average length	0.79 m
Amplitude	$39.2 \cdot 10^{-3}$ m

4.3.5 The Ripple Regularity Index (RRI)

Visually, the bed forms show a great variety in regularity. Here, an objective way to quantify the regularity of a ripple pattern is proposed, using the so-called Ripple Regularity Index (RRI). The key components to calculate RRI are image rotation and summation of columns of the image matrix. A rotational diagram is obtained, where the angular spectrum shows distinct peak that are characteristic for the ripple pattern. Like in a Fourier transform, periodic structures show up as distinct peaks, and the amplitude is a measure for the ripple amplitude, while the peak location is a measure for the ripple orientation. This method closely resembles the Radon Transform.

Here, only a brief description is given and illustrated by referring to the Figures 22 to 24. The image was rotated by a certain angle around its center and cropped to a square area of 4x4 meter. Next, the columns were summed. Depending on the rotation angle, certain periodic patterns benefit, while others cancel. The high frequency components are clearly visible in Figure 22B, where the image rotation angle equals 99 degree, i.e. the ripple orientation is parallel to the columns of the image matrix. In Figure 22A, the image was rotated by 23 degree: the high frequency ripples are on average zero, resulting in a low frequency pattern. The two orientations of 99 degree and 23 degree represent the dominant angles found in the Fourier analysis. By repeating this process, and rotating the image from 0 to 180 degrees in steps of 1 degree, the rotational diagram is obtained, as shown in Figure 23A.

Next, the standard deviation along the columns of the rotational diagram for each orientation, as shown in Figure 24, was calculated. The peaks correspond to dominant frequencies. As expected, high frequency patterns shows narrow peaks, while low frequency patterns show a broad peak. The Ripple Regularity Index (RRI) is defined as:

$$RRI = \frac{\sigma_{max} - \sigma_{min}}{2 \cdot \sigma_{mean}} \quad (19)$$

Here σ_{max} is the maximum standard deviation, σ_{min} is the minimum standard deviation, σ_{mean} is the mean standard deviation. A regular, periodic patterns such as a sine function has an RRI of 1, while a random patterns has an RRI of 0. High frequency ripples having additional low frequency components and/or random patterns cause an $RRI < 1$.

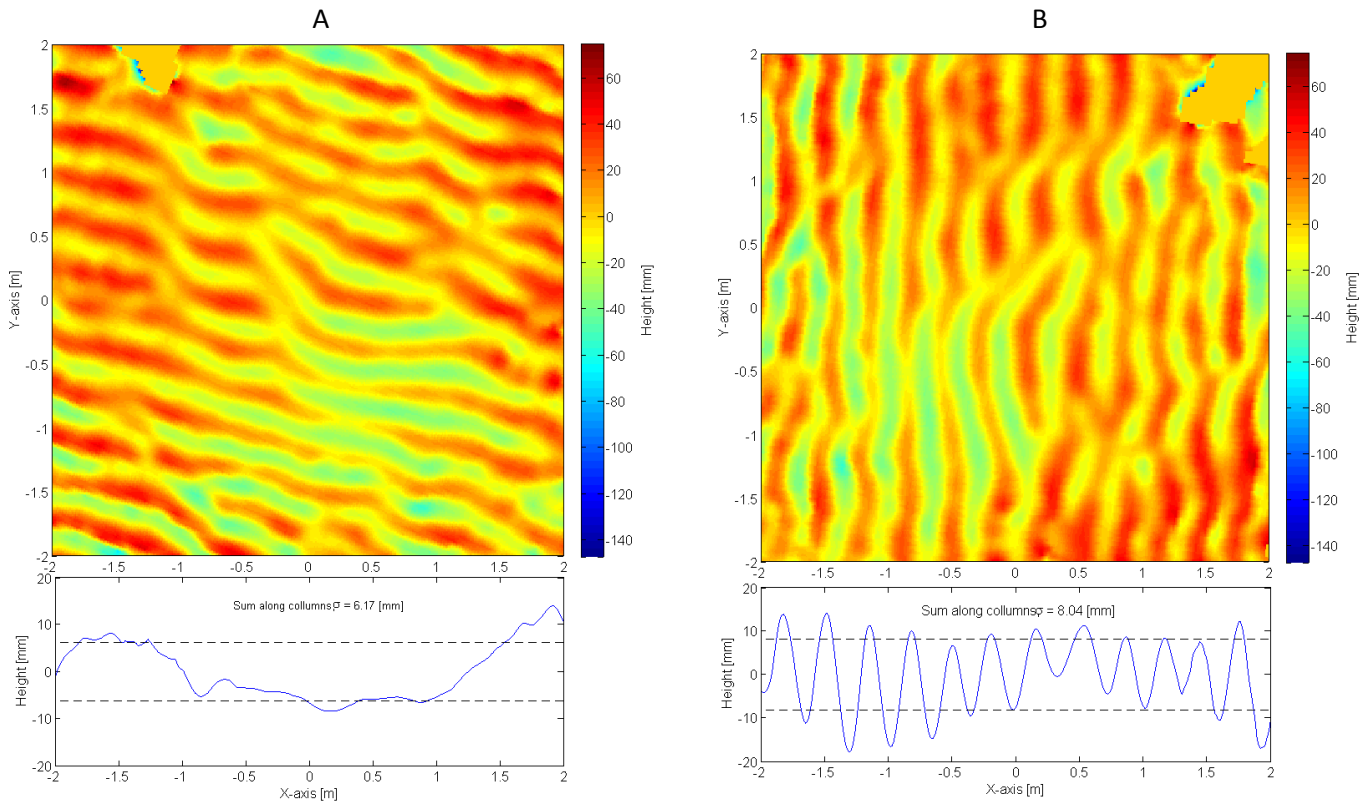


Figure 22. For each rotated image, the columns were summed and the average value was calculated. (A) shows the result when the image is rotated over an angle of 23 degrees, while (B) shows the result for an image rotation angle of 99 degrees. Notice the difference in periodicity.

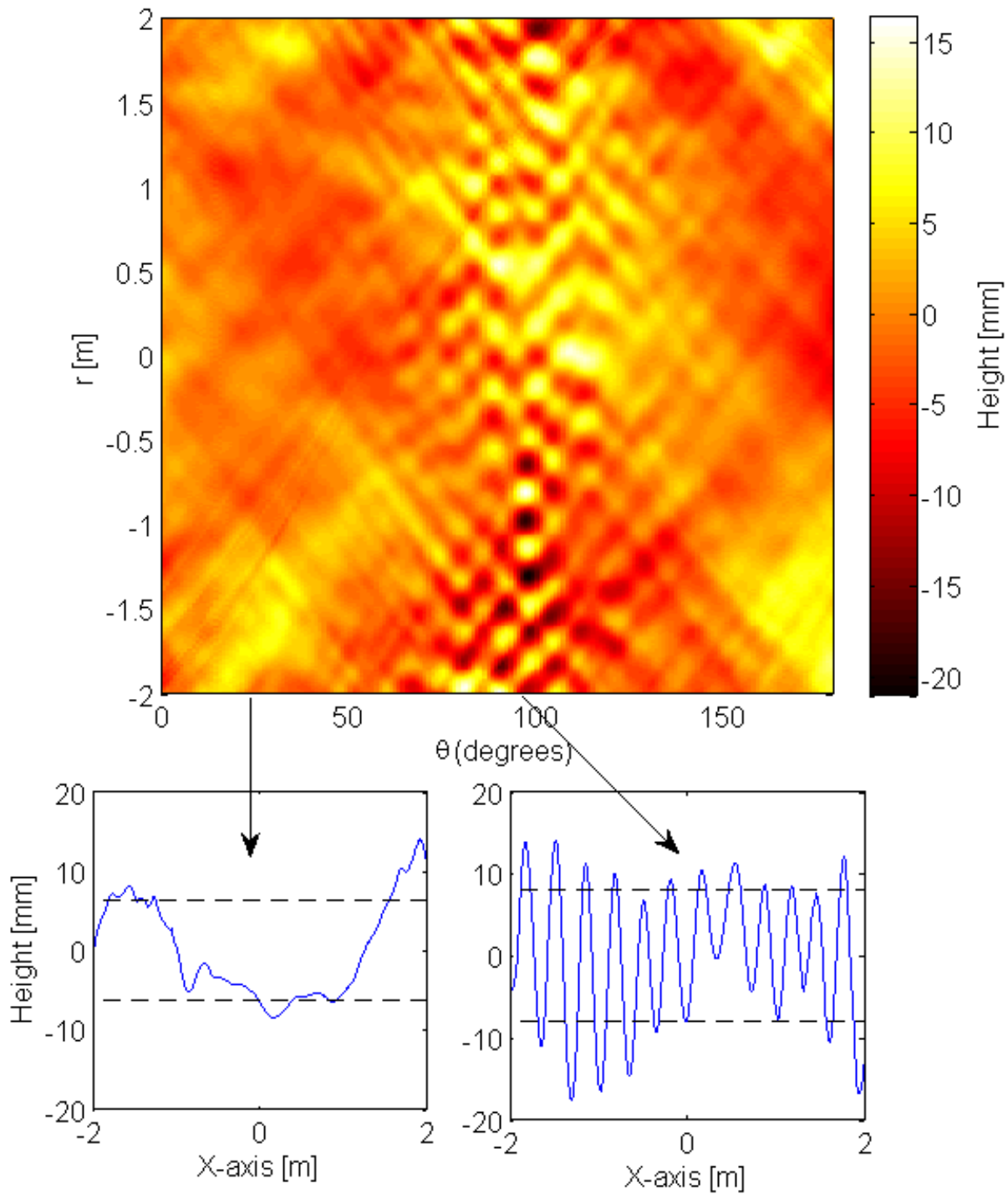


Figure 23. (A) The full rotational diagram of the sonar image. (B) Two examples of vertical transects: the low frequencies at 23 degrees versus the high frequencies at 99 degrees, the *standard deviation* is indicated by the dashed lines.

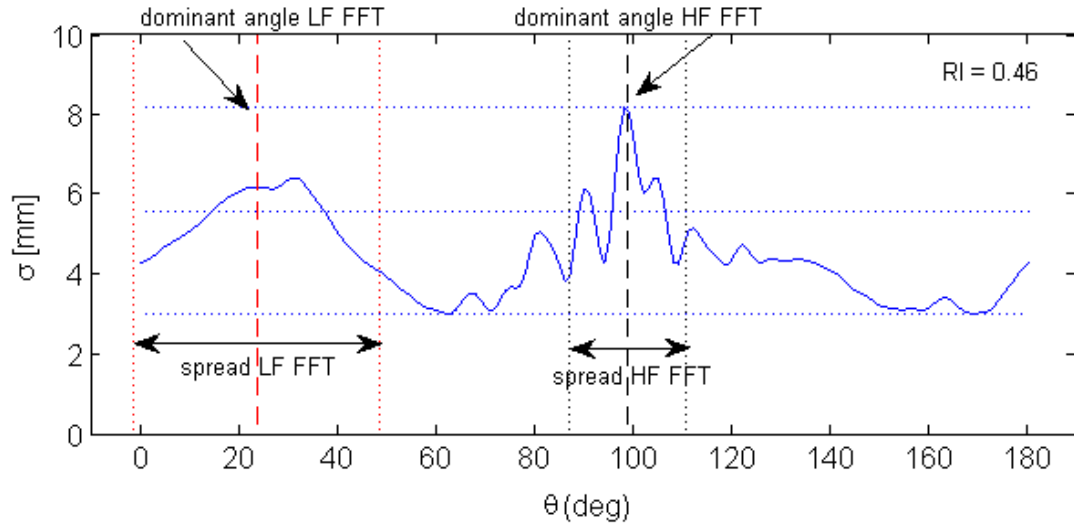


Figure 24. The standard deviation $\sigma(\theta)$ for each column (θ) of the rotational diagram. The results from the FFT-analysis were added, both the dominant angles and the angular spread, that coincide with the peak of the $\sigma(\theta)$. The Ripple Regularity Index (RRI) is found to be 0.46 for this example.

4.3.6 Hydrodynamic parameters

In this section the calculation of the wave height, wave angle, flow velocity, wave period and other hydrodynamic parameters are described. Parameters were computer for each 15 minutes of data, for a better comparison with the sonar images.

The mean wave angle was calculated with the orientation of the first eigenvector. The spread of the angle was calculated using the square root of the relative contribution of the second eigenvector. The maximum value of the spread is 40.5 degrees, corresponding with an isotropic velocity field.

For the calculation of the wave height, a second order trend was first removed from the sea surface elevation data to remove tidal variations. The high frequency waves were separated with a bandpassfilter (from 0.05Hz up to 1Hz), and used to calculate the relative wave height:

$$\frac{Hm0_{HF}}{h} \quad (20)$$

Were $Hm0_{HF}$ is the high frequency wave height and h is the water depth. The calculation of the orbital motion (equations 1-3) requires the wavelength (L). The wavelength was calculated using the dispersion equation (Masselink et al., 2011):

$$L = \frac{g}{2\pi} T^2 \tanh\left(\frac{2\pi h}{L}\right) \quad (21)$$

Here h is the water depth, g the gravitational acceleration, T is a single wave period and L is the wavelength. To approximate L , the script of *G.R. Marinez (2006)* was used. The dispersion equation was solved with the Newton-Rapshon method. Now all the variables for the ripple classification of *Clifton (1976)* are known. A number of hydrodynamic parameters were used to calculate a measure of sediment mobility. Here, the equations to calculate the non-dimensional shields parameters were used. The wave shields parameter (θ_w) was calculated from the significant orbital velocity ($u_{b,1/3}$):

$$u_{b,1/3} = 2 \sqrt{S_u^2 + S_v^2} \quad (22)$$

Where S_u^2 and S_v^2 are the *rms* bottom wave orbital velocity. Both were calculated from cross shore and longshore velocities. To calculate the velocities a spectral filter, from zero up to the Nyquist frequency, was applied. Now the wave shields parameter was calculated:

$$\theta_w = \frac{0.5f_w u_{b,1/3}^2}{(s-1)gD} \quad (23)$$

Here s is the nondimensional sediment density parameter, g is the gravitational acceleration, and f_w is defined as:

$$f_w = \begin{cases} \exp \left[5.213 \left(\frac{2.5D}{A_{b,1/3}} \right)^{0.194} - 5.977 \right], & \frac{A_{b,1/3}}{2.5D} > 1.57 \\ 0.3; & \frac{A_{b,1/3}}{2.5D} \leq 1.57 \end{cases} \quad (24)$$

Here $A_{b,1/3} = u_{b,1/3}T/2\pi$. The shield current parameter (θ_c), used to represent the effect of mean current on ripple processes, is defined as:

$$\theta_c = \frac{C_D U_z^2}{(s-1)gD} \quad (25)$$

Where U_z is the mean flow measurements and C_D is the drag coefficient:

$$C_D = \left[\frac{0.40}{\ln \left[\frac{z}{D/12} \right]} \right]^2 \quad (26)$$

Here z is the estimated elevation of the mean flow measurements. The current and wave shields parameters are responsible for the mobilization of the bed sediment (*Nelson and Voulgaris, 2014*). The value for C_D was estimated at 1.9E-3. For the dataset of *Nelson and Voulgaris, 2014* C_D was estimated at 2.0E-3.

5. Results

5.1 Overview of the dataset

Figures 25, 27 and 28 present an overview of wave and ripple characteristics during the field campaign for each 15 minutes for the high tides with available ripple measurements. The Fourier analysis results, i.e. ripple length and ripple orientation, are compared with hydrodynamic data and shields parameters. During most tides correlations between hydrodynamics and ripple characteristics are found.

The relative wave height varies between 0.3 and 0.6 throughout the selected measurements (Figure 25a). The wave angle was between -18 and 5 degrees with respect to shore normal (Figure 25b), where negative angles are waves arriving from the southwest. The ripple orientation shows more variation than the wave angle, varying between -48 and 49 degrees (Figure 25c), orientations are comparable to the wave angle. The ripple length varied between 0.28 and 0.81 meters (Figure 25d). Compared to the ripple orientation, the wave angle shows much less variation, the correlation between these two parameters is weak, R^2 is 0.18 and RMSE is 13.5 deg.

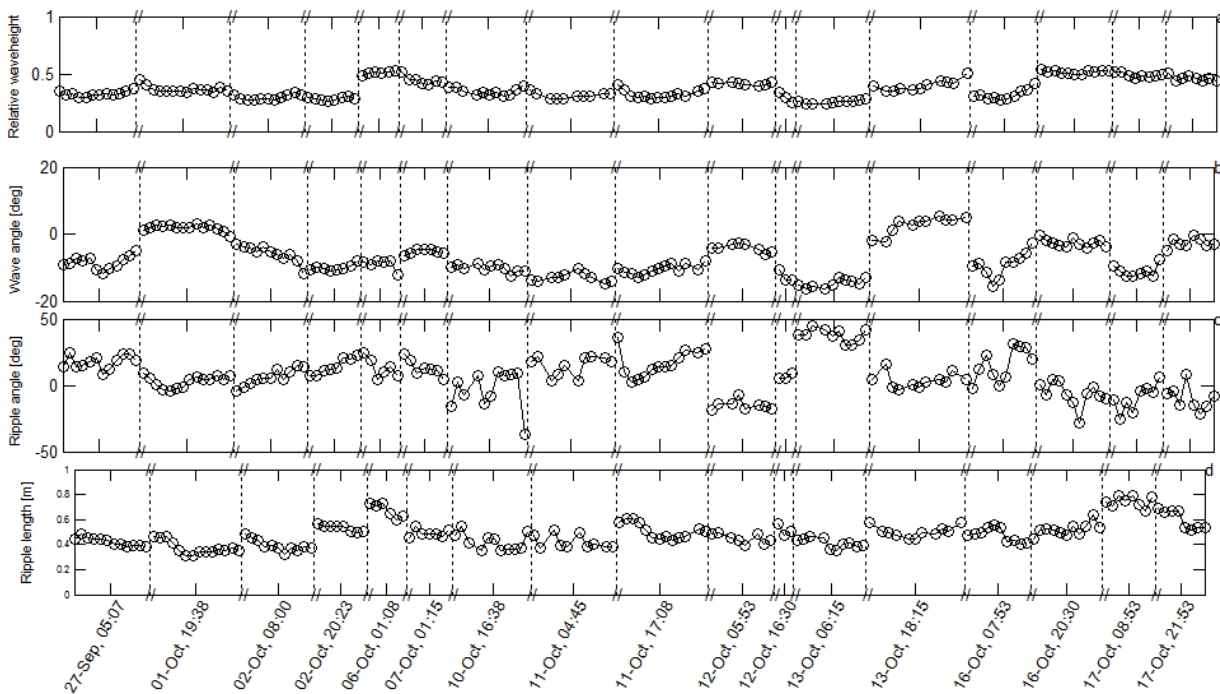


Figure 25. Results from the Fourier analysis and several hydrodynamic parameters from the Rig. From top to bottom: (a) Relative wave height, (b) Wave angle, (c) The weighted average ripple orientation and (d) The weighted average ripple period. The labels at the time axes are set in the middle of each high tide, notice that not all high tides have measurements (there is for example a gap between 27 September and the first of October). The vertical dashed lines indicate the different tidal periods.

The correlation of the ripple length (λ) and the relative wave height (H_{rel}) is shown in Figure 26. If the relative wave height increases also the ripple length increases, in agreement with *Clifton 1976* and *Goldstein et al. 2013*. The following linear relation is found: $H_{rel} = 1.27 * \lambda$. The correlation has a R^2 value of 0.31 and a RMSE of 0.086m. Other variable are expected to be important for the formation of the ripple characteristics as well.

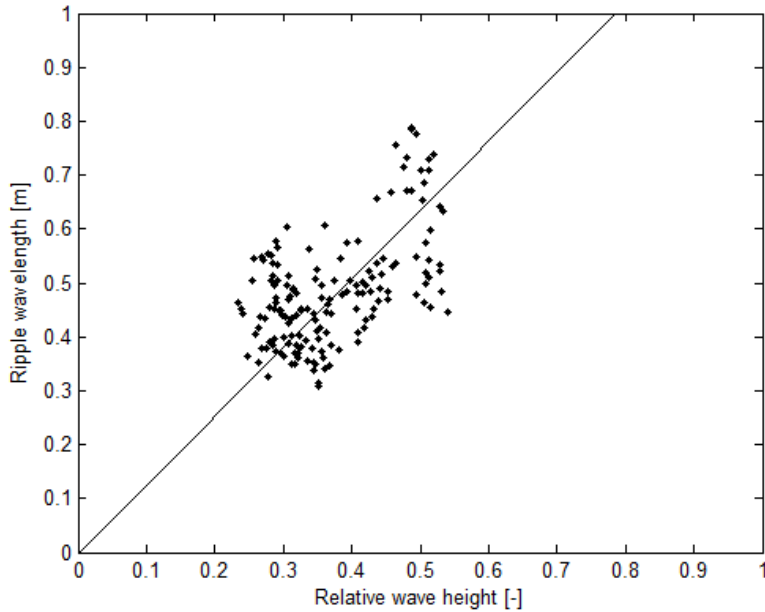


Figure 26. Relation between the relative wave height and the average ripple wavelength ($H_{rel} = 1.27 * \lambda$).

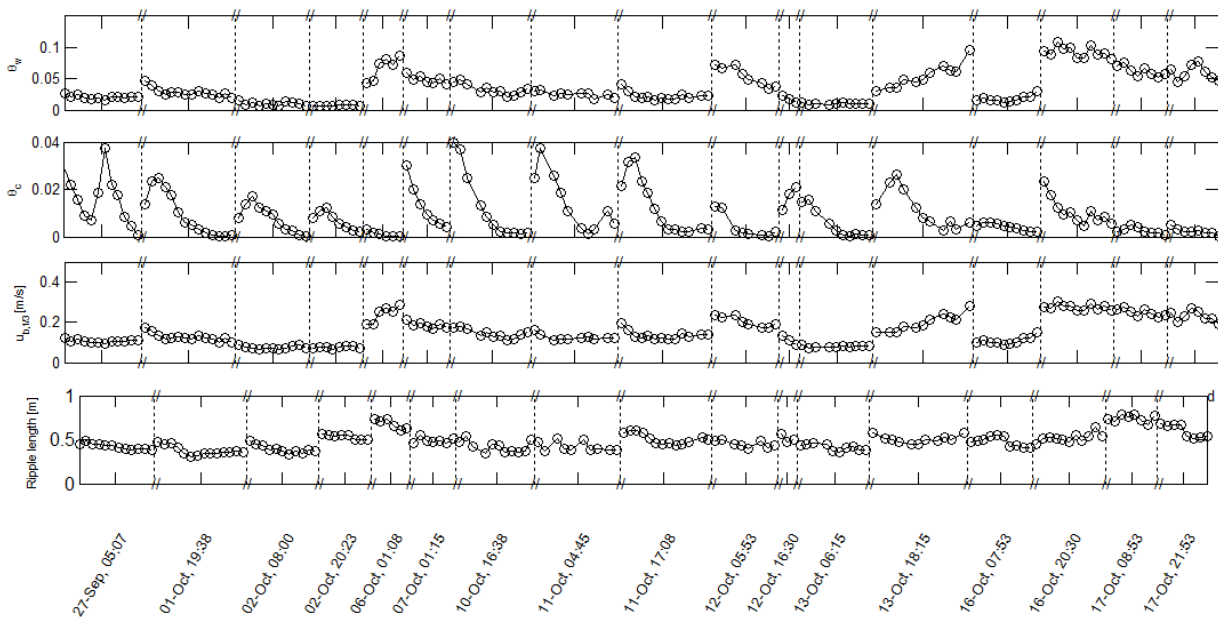


Figure 27. An overview of the shields parameters and the significant orbital velocity as defined in *Nelson and Voulgaris 2014*. Current measurement originate from MiniFrame13. From top to bottom: (a) the wave skin friction Shields parameter, responsible for the mobilization of bed sediment by waves, (b) the current skin friction Shields parameter, a measure for the mobilization of bed sediment by currents, (c) the significant orbital velocity and (d) the weighted average ripple period.

Figure 27 indicates the shields parameters and the significant orbital velocity as well as the ripple length. The wave skin friction shields parameter and the current skin friction parameter are responsible for the mobilization of bed sediments. The current shields number (θ_c) varies with variations in the mean current. Other parameters (C_D, s, g, D) are constants. The wave shields number (θ_w) varies with the significant orbital velocity ($u_{b,1/3}$) and the wave friction coefficient (f_w). The wave friction coefficient depends on the significant orbital velocity and the wave period. There are also constants: s, g, D .

A higher shields number indicates that sediment is brought into suspension more easily. The critical shields parameter (θ), as used in Nelson and Voulgaris (2014) equals 0.05. When there is more sediment into suspension the bedforms can change faster, the adaptation time to new conditions is expected to be smaller. During the rising tide there are no bedforms present, they have been erased by breaking waves and swash, so, each high tide new bedforms are formed. Whether they can adapt to the constantly changing water levels, wave conditions and currents, depends on the mobility of the sediment.

θ_w shows more variability between the tides compared to θ_c . This is expected, as θ_w depends on the wave conditions. It seems that ripple length increases with a higher shields parameter. The highest values for θ_c are often found at the beginning of the measurements: based on this parameter it is expected that ripples change mainly during the beginning of the high tide. As MiniFrame13's location is further inland the rising tides arrives slightly later, the initially lower water levels during the rising tide is expected to correspond with higher current shields parameters. The current shields parameter at the location of the sonar frame is expected to follow the same pattern, though earlier. During falling tide higher current shields parameters are expected, but the water level is then already too low for the sonar to collect meaningful measurements.

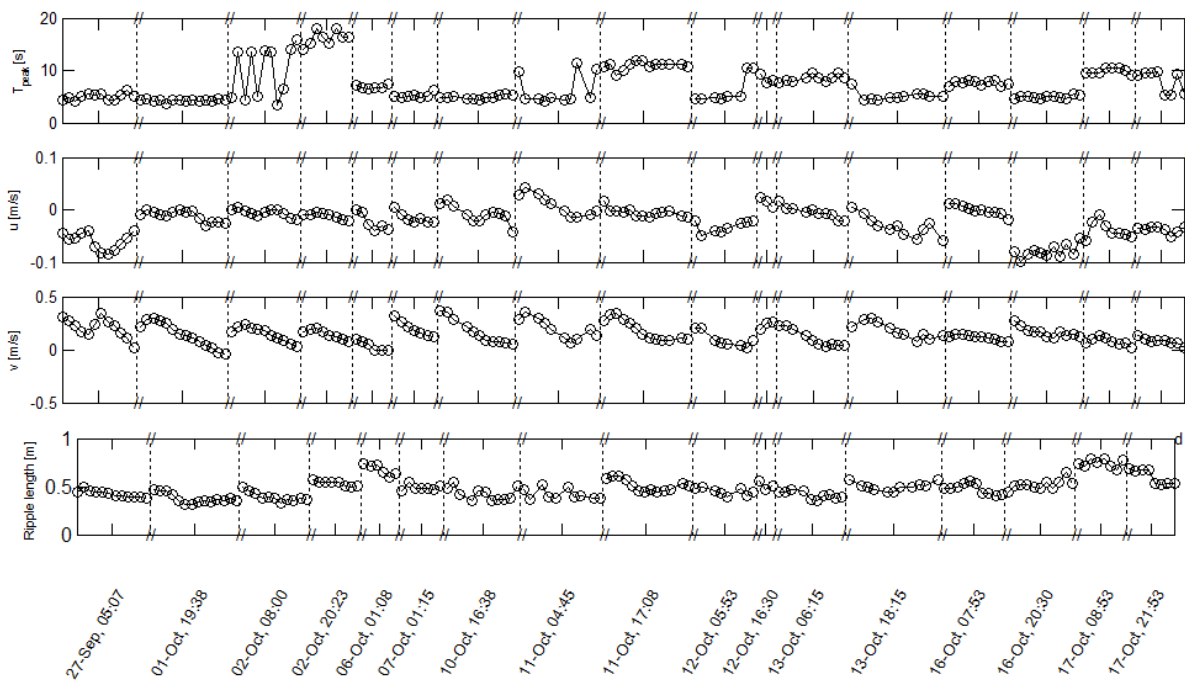


Figure 28. An overview of (a) the peak period of the waves, (b) cross-shore velocity, (c) longshore velocity and (d) the weighted average ripple period (λ).

The peak period of the waves varies between 4 and 19 seconds (Figure 28a). The cross-shore velocity's are small, between -0.1 and 0.05 m/s. Negative cross-shore velocities are directed seawards, positive cross-shore velocities are directed landwards. The longshore velocity shows more variation, with velocities up to 0.40m/s towards the north. The first measurements of a high tide, usually have the highest longshore velocities. At the end, the longshore velocity is usually the smallest. The experimental data of the ripple length shows no clear correlation with these parameters.

Table 1 shown an overview of the correlation coefficient R^2 of the ripple length with various parameters. The best correlation between the ripple length and ripple amplitude, $U_{b_{1/3}}$ and the relative wave height H_{rel} . The correlation to the relative wave height was already discussed above. The correlations to ripple amplitude and $U_{b_{1/3}}$ will be discussed in the sections.

Table 1. Correlation of the ripple length (λ) with various parameters (Figures 25, 27 and 28 and others).

Correlation coefficient for the ripple length	
	R^2
Ripple Amplitude	0.74
H_{rel}	0.31
Wave angle	0.013
Ripple orientation	0.082
θ_w	0.24
θ_c	0.035
$U_{b_{1/3}}$	0.35
T_{peak}	0.060
Cross-shore velocity	0.034
Longshore velocity	0.044

One parameter is not discussed in these overview figures: the ripple regularity. The ripple regularity is found not to correlate with any parameter. As this ripple characteristic is not calculated from the FFT, the rotational diagram methods will be compared to the FFT in the next chapter. An overview of the ripple regularity is presented in Chapter 5.3.

5.2 Ripple Index

Figure 29 shows a clear relation between ripple amplitude and ripple wavelength. Larger ripple amplitudes correspond to larger ripple wavelengths. The slope represents the ripple steepness. The ripple index (RI) is defined as $1/\text{slope}$, a RI of 17.1 is found. The standard deviation of the correlation is 0.018. According to the classification table of *Dumas et al. 2005* (Figure 8) wave ripples have a RI between 8 and 12. Here, a RI of 17 is found, which is more appropriate for current ripples.

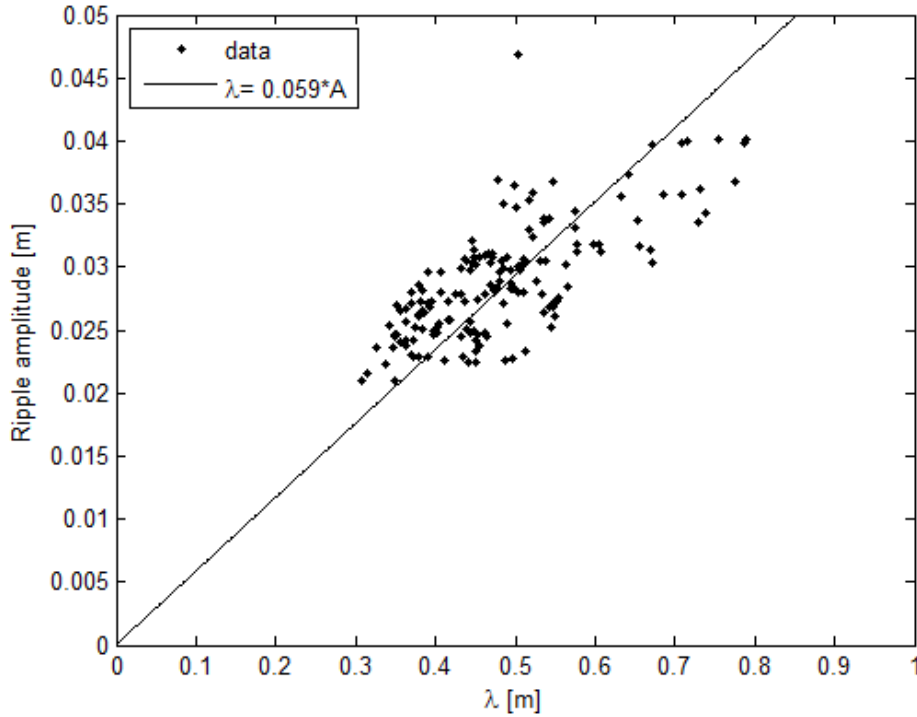


Figure 29. A linear relation (solid line) between ripple amplitude and ripple wavelength (dots) is found. The slope corresponds to a ripple index of 17.1.

5.3 Overview of the Ripple Regularity Index

The results of the Rotational diagram method are compared with the Fourier analysis (Figure 30). The Rotational diagram method is an objective method to quantify and define the ripple regularity index. The dominant angle of the low/high frequencies and spread of the orientation is comparable to the orientations found for the Rotational diagram method. Often, low and high frequency ripples are approximately orthogonal, although sometimes also a low frequency component can be found in the same direction as the HF- ripples.

In Figure 31 the results of the rotational diagram method are shown for the entire dataset. Figure 31A shows a histogram of the Ripple Regularity Index (RRI). The Rotational diagram, shown in Figure 31B, visualises the (ir)regularity of the ripples. The two examples show a regular and irregular ripple pattern. Figure 30C shows the corresponding sonar images. On average, the ripple patterns have an RRI of 0.47. Images that have a low RRI number of 0.27 are shown on the left hand side of the columns B,C and are intuitively indeed judged as irregular. In contrast, very regular ripple patterns having an RRI = 0.71 are shown in the right column.

The ripple patterns now have an objective regularity number. This method of determining an RRI for ripples is new and no reference material could be found. The RRI value is difficult to compare to a symmetry index, defined by *Dumas 2005* as the ratio of the horizontal length of the stoss versus the lee sides of 2D ripples. In contrast the RRI applies to a 3D pattern. Perfect regular ripple patterns have RRI value of 1. Even the most regular pattern, with an RRI value of 0.71, is not perfectly regular. Most ripples can be named "irregular".

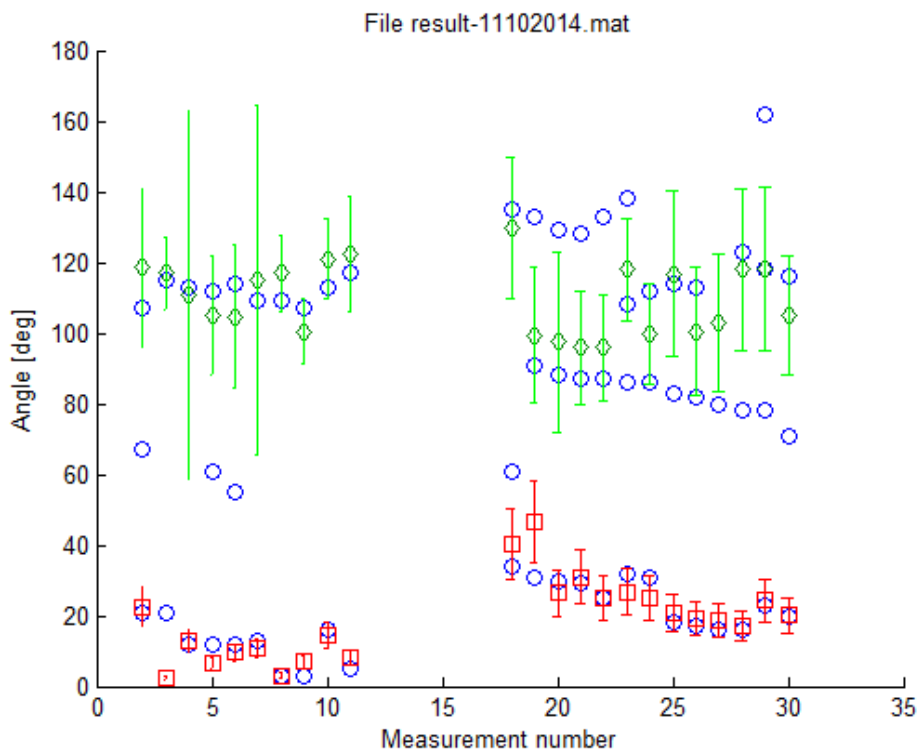
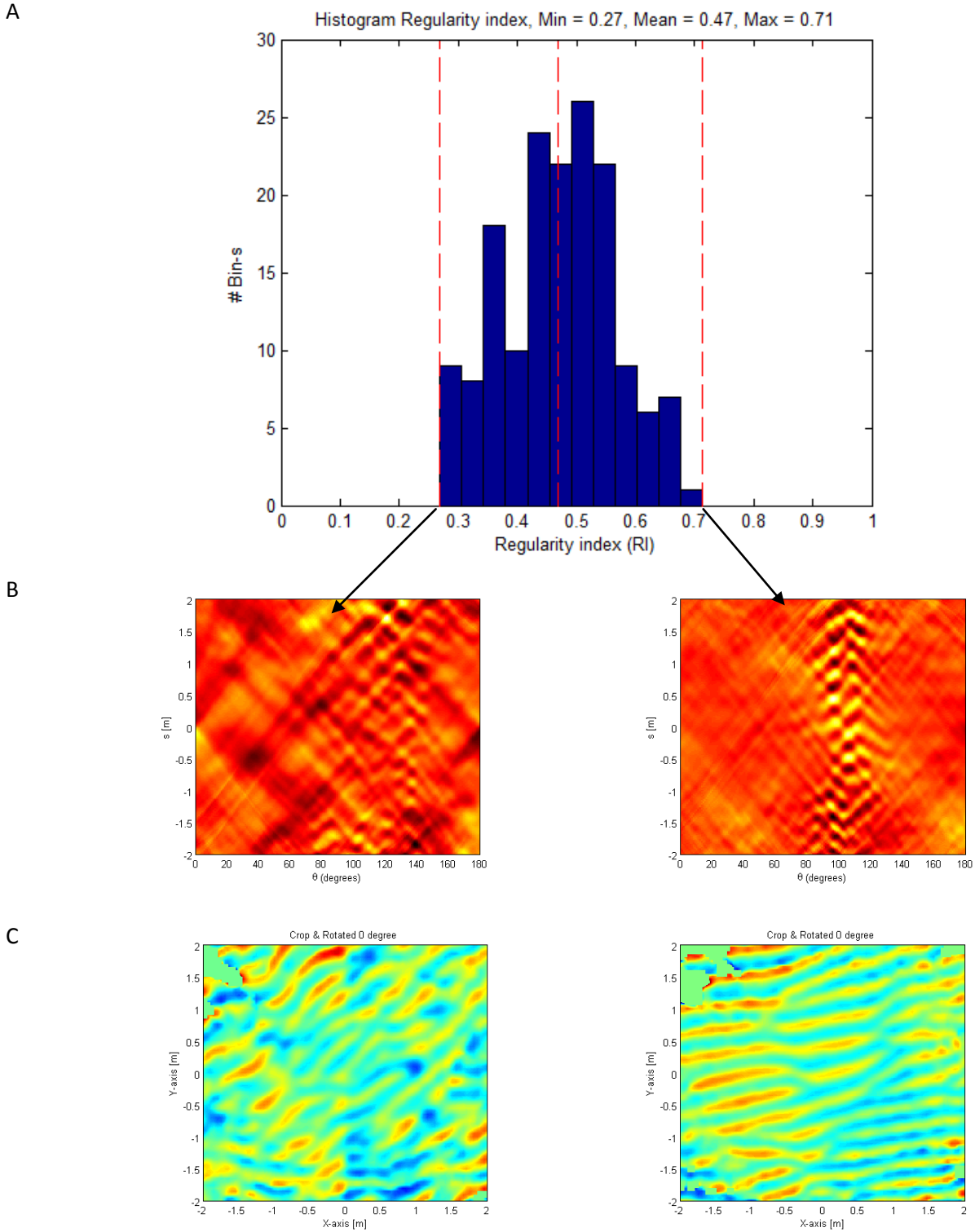


Figure 30. The results of the FFT method and the Rotational diagram method for one tidal period, the data set 11-10-2014, are shown. The Rotational diagram method peaks are represented as blue circles. For each measurement two or three peaks are found. Green diamonds represent the FFT high frequency peaks and the red squares the LF FFT peaks. The FFT calculated angular spread is indicated by the error bar.

Figure 31. Results from the Rotational diagram method, with (a) a histogram of the Ripple Regularity Index (RRI) for the entire data set, (b) two examples of the outcome at a ripple regularity at 0.27 and 0.71 and (c) the corresponding ripple data.



5.4 Ripple classification

The high RI, found in Chapter 5.2, might suggest these ripples are current ripples. Figure 32 shows a clear correlation with the diameter of orbital motion, the ripples can thus be classified as orbital. The ripples are plotted according to the Classification of Clifton (1976). In Figure 32A the ripples are classified as according to the regularity index, where 1 implies a regular pattern and zero a random pattern. In general the ripples are irregular, in agreement with O'Donoghue (2006). According to O'Donoghue (2006) grain size is the primary factor determining the regularity of the ripples. It was found that for the grain sizes larger than 0.3mm irregular ripples occur. The RRI shows scatter, no clear pattern can be observed although a tendency is observed where regular ripples favor small values of d_0 . In other words: the regularity of the ripples does not determine the ripple type (orbital, suborbital or anorbital), in agreement with O'Donoghue (2006). Most of the ripples show a correlation between diameter of orbital motion and ripple length, which is characteristic for orbital ripples. A small group does not follow this pattern. These ripples are either not in equilibrium with the hydrodynamic conditions (i.e. hysteresis) or different ripple types. There is no clear separation between ripples in equilibrium and out of equilibrium. The classification of Clifton 1976 is insufficient to classify this dataset.

In Figure 32B the same figure is plotted, now the ripples are classified in two groups: measured during rising and during falling tide. Austin et al., 2007 found ripples to be in equilibrium with the hydrodynamic forcing during rising tide and out of equilibrium during falling tide. This classification could possibly explain our outliers, but in contrast to Austin et al., 2007 no relation with rising and falling tide is found. It appears that no steady state is reached, the hydrodynamic conditions change fast compared to the relaxation times of the ripple formation.

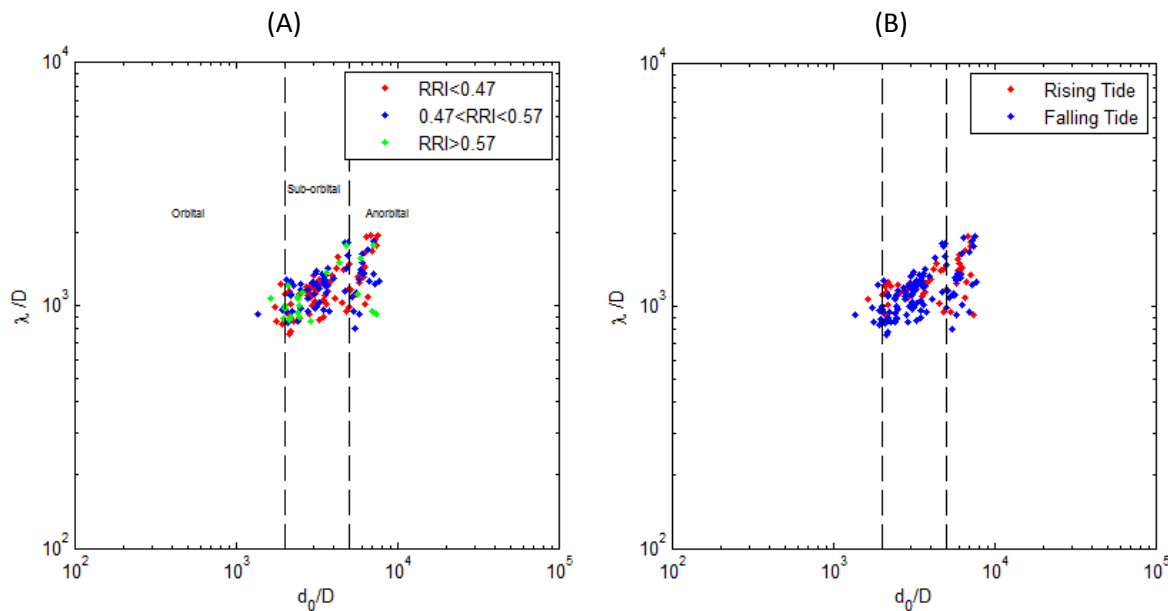


Figure 32. Classification of ripples according to Clifton 1976. (A) Ripples are subdivided as regular ($RRI > 0.57$), normal ($0.57 > RRI > 0.47$) and irregular ($RRI < 0.47$). (B) Ripples are subdivided in two groups: rising and falling tides. According to Austin et al., 2007 ripple are in equilibrium during rising tide.

In Figure 33 the wave orbital velocity is plotted vs. skewness, asymmetry and longshore current. The skewness ranges between 0.04 and 0.8 with a mean value of 0.43. The asymmetry ranges between -1.1 and 0.08 with a mean value of -0.41, indicating asymmetric waves which have an interaction with the bottom. The longshore current is up to 0.4m/s. Hay et al (2005) investigated the importance of wave skewness and wave asymmetry according to the concept of Clifton (1976). It was found that mainly ripple regularity is depending on the diameter of orbital motion. Here, low wave-orbital velocities are measured when ripples are relatively regular. Higher wave orbital velocities generally have lower RII values. Besides these observations the ripple regularity does not seem to depend on skewness, asymmetry or longshore currents.

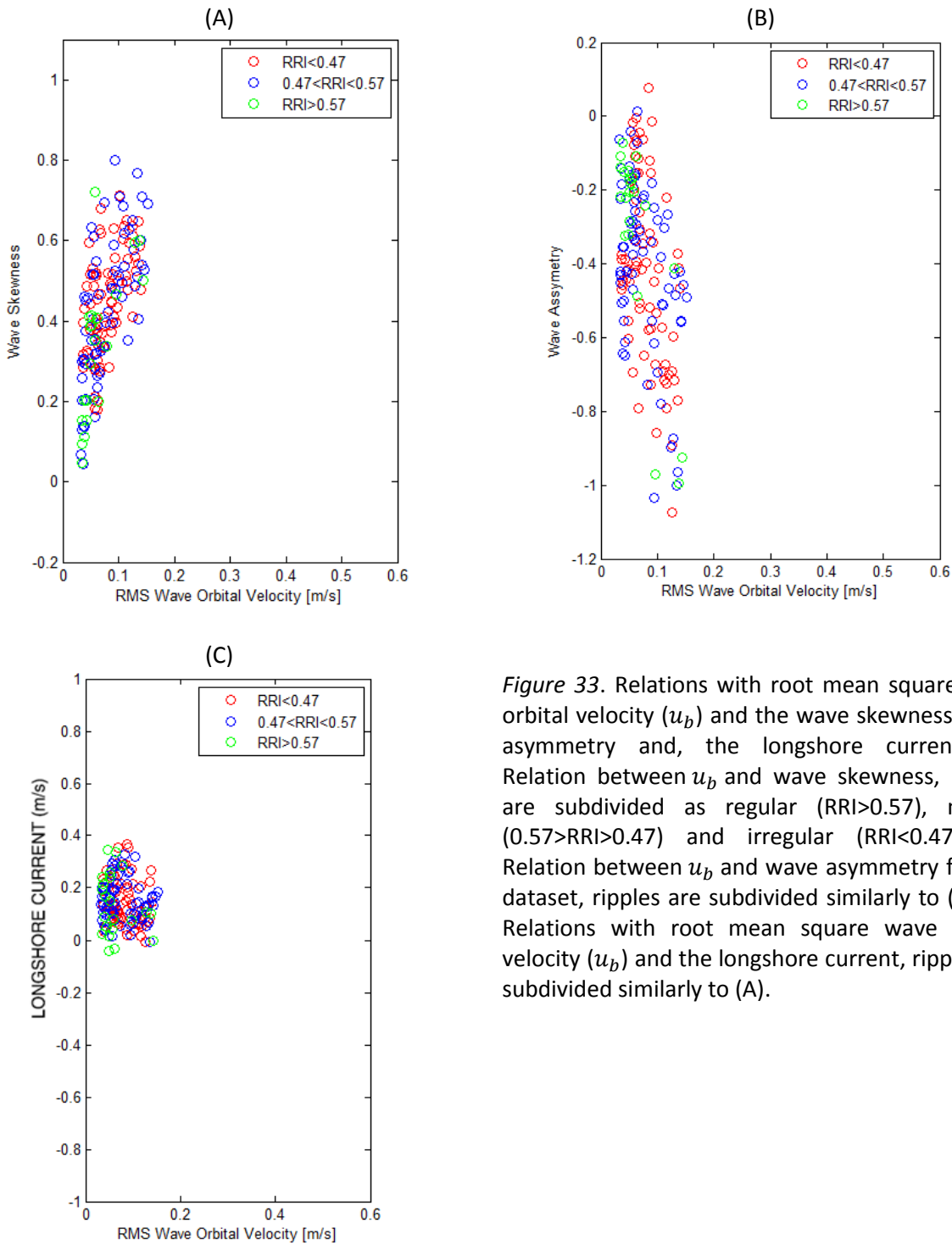


Figure 33. Relations with root mean square wave orbital velocity (u_b) and the wave skewness, wave asymmetry and, the longshore current. (A) Relation between u_b and wave skewness, ripples are subdivided as regular (RRI>0.57), normal (0.57>RRI>0.47) and irregular (RRI<0.47). (B) Relation between u_b and wave asymmetry for this dataset, ripples are subdivided similarly to (A). (C) Relations with root mean square wave orbital velocity (u_b) and the longshore current, ripples are subdivided similarly to (A).

6. Discussion

Field measurements

The field measurements were conducted at one location at the Sand Motor. The study thus has a limited measurement area: the +/-6m diameter of the sonar. The spatial variability of ripple structure on relatively short distances (>6m) are thus not captured with the measurements. The diameter of the sonar also limits the detection of larger ripple structures, as a good FFT requires several lengths of the ripple period.

The tilting of the frame has a minimum effect on the sonar measurements, as a filter for the slope is applied. The change in angle causes a slightly different distribution of the measurement points over the rippled bed. The tilting of the frame affected mainly the current measurements. Therefore, the measurements of the cross-shore and longshore measurements come from Mini13, which is located several meters further onshore. Currents show a large longshore variability, this can be observed in the overview of the dataset. The current shields parameter shows a peak, which is expected to be late compared to the frame. A good relation between currents and parameters with currents, and ripple parameters is not found.

Results compared to literature

Figure 34A compares the dataset with ripple length predictors of *Goldstein et al., 2013*, *Nelson et al. 2013* and *Wiberg and Harris, 1994*. Formula 8 is the formula used by *Goldstein et al., 2013* which is based on several flume experiments and field data of multiple sites (dark blue line in Figure 34A). The subdivision between a flume experimental predictor and a field measurement predictor is made by *Nelson et al., 2013*. The field measurement predictor is for irregular waves, in contrast to the flume experiment predictor. Formula 13, from *Nelson et al., 2013* is based on field measurements and indicated by the red line in Figure 34A. The predictor of *Wiberg and Harris, 1994* (formula 4) is based on laboratory experiments and indicated by the blue line in Figure 34A.

In contrast to the other predictors the predictor of *Nelson et al. 2013* shows a weakly nonlinear relation with the diameter of orbital motion and grain size. The predictor of *Goldstein et al., 2013* slightly over predicts the wavelengths. The predictor *Wiberg and Harris, 1994* shows a similar relation though ripple length are much larger than the predictor of *Goldstein et al., 2013* and the data points.

In Figure 34B the predictions for ripple steepness of *Goldstein et al., 2013* and *Nelson et al., 2013* are compared. Both predictors show the same trend: the ripple steepness has a constant value. The predictor of *Goldstein et al., 2013* predicts higher steepness values than *Nelson et al., 2013*. The predictors deviate from the measured steepness, this could be caused by the unique conditions at the Sand Motor. The Sand Motor data (black dots) plots in the same range and shows more variability compared to the predictors (coloured dots).

Based on all field measurements and flume experiments a histogram of the ripple steepness is shown in Figure 35, according to *Goldstein et al., 2013*. The peak found at 0.15 represents steep ripples while the peak at 0.01 represents 'hummocky' ripples. The steepness found for this research equals 0.06, close to the steepness of 'hummocky' ripples.

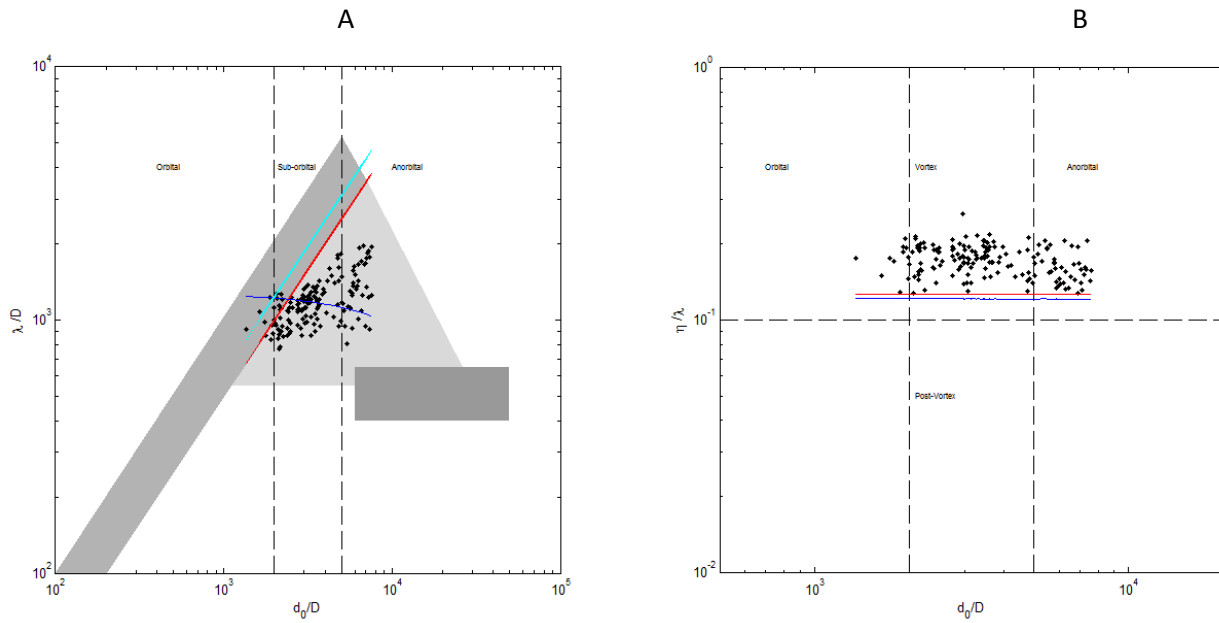


Figure 34. Comparing the ripple data with predictors of *Nelson et al., 2013*, in dark blue, (for wave ripples) and *Goldstein et al., 2013*, in red (large dataset). Also the relation for wave ripples of *Wiberg and Harris, 1994* is included in blue. (A) The grey areas are plotted according to *Masselink et al., 2007*. Ripples scaling with the diameter of orbital motion plot in the grey area (orbital), ripples not scaling with the diameter of orbital motion plot in the dark grey area (anorbital) and ripples in the light grey area are sub-orbital. (B) For both predictors a constant steepness value, slightly higher than the this dataset, is found.

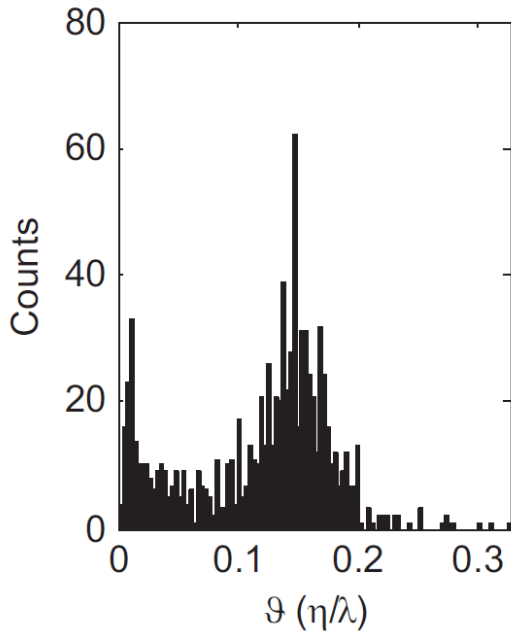


Figure 35. Steepness histogram of *Goldstein et al., 2013*. On the x-axis the steepness value and on the y-axis the number of counts is plotted.

The field experiment of Masselink et al., 2007 was also in the intertidal zone, with instruments below the mean high tide neap level. The ripples were measured with two Sand Ripple Profilers (SRP) in cross-shore direction. In contrast to this study ripple characteristics were derived from 2D ripples. The conditions and results of the measurements are summarized in Table 2. The slope is comparable with these measurements, e.g. 1:30. The grain size of Masselink et al., 2007 is larger, 0.40mm against 0.69mm. In contrast to this research steep vortex ripples are found. Besides differences in hydrodynamic conditions it can be expected that the grain size is the main factor determining the ripple characteristics.

Table 2. Overview of the results and conditions during the measurements of Masselink et al., 2007.

Parameter	
Grain size	0.69mm
Steepness beach	1:33
Ripple height	~5cm
Ripple length	~35cm
Ripple steepness	~0.16
Ripple Classification (Clifton, 1976)	vortex

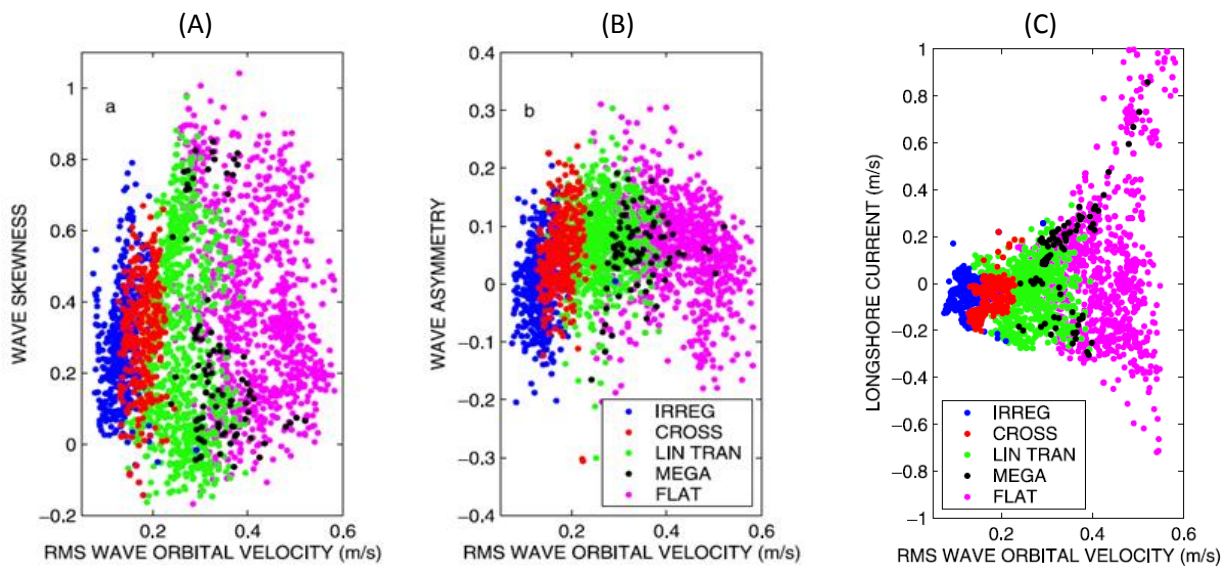


Figure 36. (A) Relation between u_b and wave skewness according to Hay et al., 2005, classification according to Clifton, 1976: irregular ripples (blue), cross ripples (red), linear transition ripples (green), lunate megaripples (black), and flat bed (magenta). (B) Relation between u_b and wave asymmetry according to Hay et al., 2005, similar classification as (A). (C) Relation between u_b and longshore current according to Hay et al., 2005, similar classification as (A).

Hay et al., 2005 classified the ripples as irregular, cross ripples, linear transition ripples, lunate megaripples and flat bed. These ripples are plotted in Figure 36, and can be compared to our own results in Figure 33. It can be observed that all ripples from this dataset plot within the irregular and cross ripple regime of Hay et al., 2005. They found an increase in longshore velocity spread for regular ripples, irregular ripples showed the least variability in longshore current. Megaripples and flat bed both have longshore currents higher than 0.2m/s, though for both bedform types the root mean square wave orbital velocity was much larger. Longshore velocities of this measurement campaign were up to 0.4m/s. The locally generated longshore currents show spatial variability and depend on the beach profiles.

Recommendations for future research

For the construction of the 3D sonar image several assumptions and a correction have been made. The irregular grid is interpolated to a regular grid, using a fixed box size. For the height a correction factor is applied, hereby a certain box size as reference height. There is no visual conformation for the real ripple patterns. For future research a high speed underwater camera could serve as visual conformation. With high visibility processing routines can derive ripple characteristics. Also, with a high speed camera the research can be extended as the behaviour and magnitude of sediment transport can also be derived.

7. Conclusion

Methods to quantify the 2D and 3D characteristics of ripples in the intertidal zone and relations between these characteristics and hydrodynamic conditions have been investigated at the Sand Motor. The research questions, *How can ripple characteristics be quantified in an objective way? What kind of ripples can be found in the intertidal zone? Is there a relation between ripple length, height, orientation, and the hydrodynamics? How can ripple regularity be classified in an objective and quantitative way?*, will be answered respectively.

Ripple characteristics

The ripple amplitude is calculated from the standard deviation of the 3D image. The ripple characteristics, ripple length and orientation, have been quantified by means of a FFT. Each 3D image consists of several ripple lengths and orientations. The weighted average mean ripple length and orientation are used as objective ripple characteristics for further analysis.

The rotational diagram method is an alternative method to characterise a 3D image. The method has similarities to the FFT. The ripple regularity index, a quantitative method, to quantify the regularity of a 3D ripple pattern, is derived from a rotational diagram. The Fourier analysis and rotational diagram method on the 3D sonar images have provided a new way to analyse the ripple patterns of the intertidal zone.

Ripple classification

Most ripples behave as orbital ripples. This is to be expected considering the large grain size (Goldstein et al., 2013). Classification schemes of previous investigations (e.g. Clifton 1976 and Austin et al. 2007) are found to be insufficient for this dataset.

The modern ripple predictors of Goldstein et al. (2013), Nelson et al. (2013) and Wiberg and Harris (1994) show trends similar to this dataset. In contrast to the predictors the Sand Motor data shows much more variability.

Relations between ripple characteristics and hydrodynamic

Relations and correlations between various ripple characteristics and hydrodynamic parameters have been investigated. As a general observation, most parameters have a poor correlation and only in a few cases a good correlation is found. Ripple amplitude and ripple length correlate well ($R=0.71$). Also a good correlation between ripple length and relative wave height is found ($H_{rel} = 1.27 * \lambda$). This was expected according to Clifton (1976).

Ripple regularity

In this report a new method of quantifying ripple regularity is proposed: the rotational diagram method. This objective method quantifies the ripple regularity as a variable between 0 and 1, where 1 is regular. The dataset is found to be overall irregular with an average RRI of 0.47.

Acknowledgements

This study was supported by the University of Utrecht, department of Physical Geography. The author wishes to thank Gerben Ruessink and Joost Brinkkemper for the professional support of this thesis and the frequent discussions. Many thanks to Laura Brakenhoff and Florian van der Steen for sharing data and the good spirit during the fieldwork. The technicians are thanked for their support and rebuilding of the rig. Thanks to Sjoerd van Willigen for the careful reading of this thesis.

References

- Aagaard T., Jensen S.G. (2013) - *Sediment concentration and vertical mixing under breaking waves*. Marine Geology 336, 146-159.
- Bagnold, R. A. (1963) - *Beach and nearshore processes, in The Sea*. edited by M. N. Hill, 507– 553, Wiley-Interscience, New York.
- Blondeaux P., Foti E., Vittori G. (2000) - *Migrating sea ripples*. Eur. J. Mech. B - Fluids 19 p.285–301
- Clifton H.E. (1976) - *Wave-formed sedimentary structures - a conceptual model*.
- Dumas S., Arnott R.W.C., Southard J.B. (2005) - *Experiments on oscillatory-flow and combined-flow bed forms: implications for interpreting parts of the shallow-marine sedimentary record*. Journal of Sedimentary Research, 75, 501-513.
- Fredsøe J., Andersen K.H., Sumer B.M. (1999) - *Wave plus current over a ripple-covered bed*. Coastal Eng. 177–221.
- Gallagher E.J. (2003) - *A note on megaripples in the surf zone: evidence for their relation to steady flow dunes*. Marine Geology 193 p.171-176.
- Grigoriadis D.G.E., Dimas A.A., Balaras E. (2012) - *Large-eddy simulation of wave turbulent boundary layer over rippled bed*. Coastal engineering 60, 174-189.
- Hay A.E., Mudge T. (2005) - *Principal bed states during SandyDuck97: Occurrence, spectral anisotropy, and the bed state storm cycle*. Journal of Geophysical Research 110, doi:10.1029/2004JC002451.
- Hunter R.E., Clifton H.E., Phillips R.L. (1979) - *Depositional processes, sedimentary structures, and predicted vertical sequences in barred nearshore systems*. Southern Oregon Coast. J. Sediment. Petrol. 49 (3), 711- 776.
- Larcy J.R., Rubin D.M., Ikeda H., Mokudai K., Hanes D.M. (2007) - *Bed forms created by simulated waves and currents in a large flume*. Journal of Geophysical research 112.
- Masselink G., Austin M.J., O'Hare T.J., Russel P.E. (2007) - *Geometry and dynamics of wave ripples in the nearshore zone of a coarse sandy beach*. Journal of Geophysical Research 112.
- Masselink G., Hughes M.G., Knight J. (2011) - *Introduction to coastal processes & geomorphology*. ISBN: 978 1 444 122 404
- Miles J., Thorpe A., Russell P., Masselink G. (2013) - *Field observations of ripple and megaripple dynamics in the nearshore*. Coastal Dynamics p.1207-1218
- Mori N., Suzuki T., Kakuno S. (2007)- *Noise of acoustic Doppler velocimeter data in bubbly flows*. J. Eng. Mech., 133, 122– 125.
- Nelson T.R., Voulgaris G. (2014) - *Temporal and spatial evolution of wave-induced ripple geometry: Regular versus irregular ripples*. Journal of Geophysical Research: Oceans 119.
- Nielsen P. (1992) - *Coastal bottom boundary layers and sediment transport*. ISBN: 13 978 981 02 0472 3.
- O'Donoghue T., Doucette J.S., Van der Werf J.J., Ribberink J.S. (2006) - *The dimensions of sand ripples in full-scale oscillatory flows*. Coastal Engineering 53, 997-1012.
- Osborne P.D., Vincent C.E. (1996) - *Vertical and horizontal structure in suspended sand concentrations and wave-induced fluxes over bedforms*. Marine Geology 131, 195-208.
- Plant N.G., Holland K.T., Puleo J.A. (2002) - *Analysis of the scale of errors in nearshore bathymetric data*. Marine Geology 191, 71-86.
- Plant N.G., Holman R.A., Freilich M.H., Birkemeier W.A. (1999) - *A simple model for interannual sandbar behavior*. Journal of geophysical research, 104, 15755-15776.
- Ruessink B.G. (2010) - *Observations of Turbulence within a Natural Surf Zone*. Journal of Physical Oceanography 40, 2696-2712.
- Ruessink B.G., Michallet H., Abreu T., Sancho F., Van der A D.A., Van der Werf J.J., Silva P.A. (2011) - *Observations of velocities, sand concentrations, and fluxes under velocity-asymmetric oscillatory flows*. Journal of Geophysical Research 116.
- Spiegel M.R. (1974) - *Schaum's outline of theory and problems of Fourier analysis with application to boundary value problems*. ISBN: 0-07-060219-0
- Thornton E.B., Swayne J.L., Dingler J.R. (1998) - *Small-scale morphology across the surf zone*. Marine Geology 145, 173-196.
- Vincent C.E., Hanes D.M., Bowen A.J. (1991) - *Acoustic measurements of suspended sand on the shoreface and the control of concentration by bed roughness*. Marine Geology 96, 1-18.

Van Rijn, L. C., Ribberink, J. S., Van Der Werf, J., Walstra, D. J. R. (2013) - *Coastal sediment dynamics: recent advances and future research needs*. Journal of Hydraulic Research 51 (5), 475–493.

websites:

dezandmotor.nl

live.getij.nl

nl.mathworks.com/help